

Accepted by ApJ

THE KONUS-*WIND* CATALOG OF GAMMA-RAY BURSTS WITH KNOWN REDSHIFTS. II. WAITING MODE BURSTS SIMULTANEOUSLY DETECTED BY *SWIFT*/BAT.

Anastasia Tsvetkova^{1,a}, Dmitry Frederiks^{1,b}, Dmitry Svinkin¹, Rafail Aptekar^{1,†}, Thomas L. Cline^{2,*}, Sergei Golenetskii¹, Kevin Hurley³, Alexandra Lysenko¹, Anna Ridnaia¹, Mikhail Ulanov¹

Abstract

In the Second part of The Konus-Wind Catalog of Gamma-Ray Bursts with Known Redshifts (first part: Tsvetkova et al. 2017; T17), we present the results of a systematic study of gamma-ray bursts (GRBs) with reliable redshift estimates detected simultaneously by the Konus-*Wind* (KW) experiment (in the waiting mode) and by the *Swift*/BAT (BAT) telescope during the period from 2005 January to the end of 2018. By taking advantage of the high sensitivity of BAT and the wide spectral band of KW we were able to constrain the peak spectral energies, the broadband energy fluences, and the peak fluxes for the joint KW-BAT sample of 167 weak, relatively soft GRBs (including four short bursts). Based on the GRB redshifts, which span the range $0.04 \leq z \leq 9.4$, we estimate the rest-frame, isotropic-equivalent energy, and peak luminosity. For 14 GRBs with reasonably constrained jet breaks, we provide the collimation-corrected values of the energetics. This work extends the sample of KW GRBs with known redshifts to 338 GRBs, the largest set of cosmological GRBs studied to date over a broad energy band. With the full KW sample, accounting for the instrumental bias, we explore GRB rest-frame properties, including hardness-intensity correlations, GRB luminosity evolution, luminosity and isotropic-energy functions, and the evolution of the GRB formation rate, which we find to be in general agreement with those reported in T17 and other previous studies.

Subject headings: catalogs – gamma-ray burst: general – methods: data analysis

¹Ioffe Institute, Politekhnicheskaya 26, St. Petersburg 194021, Russia; tsvetkova@mail.ioffe.ru

²NASA Goddard Space Flight Center, Greenbelt, MD 20771, USA

³University of California, Berkeley, Space Sciences Laboratory, 7 Gauss Way, Berkeley, CA 94720-7450, USA

^atsvetkova@mail.ioffe.ru

^bfred@mail.ioffe.ru

†Deceased

*Retired

1. Introduction

Gamma-ray bursts (GRBs) were discovered more than a half a century ago, and their cosmological origin was established about two decades ago via identifications of the burst optical counterparts and their redshift measurements. As of 2019, cosmological redshift (z) estimates are known for ~ 500 GRBs, ranging from spectroscopic $z = 0.0087$ (GRB 980425; Foley et al. 2006) to photometric $z = 9.4$ (GRB 090429B; Cucchiara et al. 2011a) or NIR spectroscopic $z = 8.1$ (GRB 090423; Salvaterra et al. 2009).

With the GRB redshift known, it is possible to estimate the isotropic-equivalent burst energetics and transform the GRB spectral parameters and durations from the observer to the cosmological rest frame. At cosmological distances, huge isotropic-equivalent energy releases up to $E_{\text{iso}} \lesssim 10^{55}$ erg (e.g. GRB 080916C, Abdo et al. 2009; Greiner et al. 2009a) and isotropic peak luminosities $L_{\text{iso}} \lesssim 5 \times 10^{54}$ erg s $^{-1}$ (e.g. GRB 110918A, Frederiks et al. 2013) can be explained under the assumption that GRBs are non-spherical explosions: when the tightly collimated relativistic fireball is decelerated by the circumburst medium (CBM) down to the Lorentz factor $\Gamma \sim 1/\theta_{\text{jet}}$ (θ_{jet} is the jet opening angle), an achromatic break (jet break) should appear, in the form of a sudden steepening in the GRB afterglow light curve, at a characteristic time t_{jet} . Correction for the jet collimation decreases the energy releases and peak luminosities of GRBs by orders of magnitude. GRBs with known z may be used as cosmological probes, e.g., to study the expansion rate of the Universe and to investigate the observational properties of dark energy if the empirical correlations between spectral properties and energy are appropriately calibrated. GRB redshifts are also the keys to population studies: e.g., GRBs with high redshifts and their afterglows can serve as a unique probe of the first stars in the Universe.

The Konus-*Wind* (hereafter KW, Aptekar et al. 1995) experiment has operated since 1994 November and plays an important role in GRB studies thanks to its unique set of characteristics: the spacecraft orbit in interplanetary space that provides an exceptionally stable background; the continuous coverage of the full sky by two omnidirectional detectors; and the broad energy range (~ 20 keV–15 MeV, triggered mode; ~ 20 keV–1.5 MeV, waiting mode). Since the KW energy band is rather wide, the GRB peak energy E_p (the maximum of the EF_E spectrum) can be derived directly from the KW spectral data and the GRB energetics can be estimated using fewer extrapolations. This work extends the first part of the KW catalog of GRBs with known redshifts (Tsvetkova et al. 2017; T17) which provided temporal and spectral parameters, as well as broadband observer- and rest-frame energetics of 150 bursts detected in the KW triggered mode, with a sample-wide peak flux limit of $\sim 1 \times 10^{-6}$ erg cm $^{-2}$ s $^{-1}$. Updated up to the end of 2018, this sample comprises 171 GRBs with $0.1 \leq z \leq 5$.

The Neil Gehrels *Swift* Observatory, operating since 2004 November, is the primary source of precise GRB localizations allowing for subsequent optical identifications of the sources and their redshift measurements. Thanks to the high sensitivity of the *Swift*/Burst Alert Telescope (BAT; Barthelmy et al. 2005) telescope ($\sim 10^{-8}$ erg cm $^{-2}$ s $^{-1}$), the BAT sample of GRBs with known

z , which comprises ~ 380 events to date, is the largest one. However, the relatively soft spectral range of the instrument (15–150 keV) complicates GRB studies, since only for a limited fraction of soft-spectrum bursts can E_p and broadband fluences be constrained from the BAT data. Moreover, as Sakamoto et al. (2009) showed, even if the peak energy is located inside the BAT energy range, BAT still cannot derive E_p if the burst is not bright enough.

Here, we present a sample of 167 GRBs with reliably measured redshifts detected by KW in the waiting mode and, simultaneously, observed by *Swift*/BAT, from 2005 January to 2018 December. We start with a brief description of the KW and *Swift*/BAT instruments in Section 2. The burst sample is described in Section 3. In Section 4 we present the joint temporal and spectral analysis of KW and BAT data and derive the burst energetics. In Section 5 we discuss the analysis results, and the rest-frame properties of the whole sample of 338 KW GRBs with known z , the largest set of cosmological GRBs studied to date over a broad energy band. Our conclusions are summarized in Section 6.

All the errors quoted in this catalog are at the 68% confidence level (CL) and are of statistical nature only. Throughout the paper, we assume the standard Λ CDM model: $H_0 = 67.3 \text{ km s}^{-1} \text{ Mpc}^{-1}$, $\Omega_\Lambda = 0.685$, and $\Omega_M = 0.315$ (Planck Collaboration et al. 2014). We also adopt the conventional notation $Q_k = Q/10^k$.

2. Instrumentation

2.1. Konus-*Wind*

KW is a gamma-ray spectrometer designed to study temporal and spectral characteristics of GRBs, solar flares (SFs), soft gamma-repeaters (SGRs), and other transient phenomena over a wide energy range from 13 keV to 10 MeV, nominally (i.e., at launch). It consists of two identical omnidirectional NaI(Tl) detectors, mounted on opposite faces of the rotationally stabilized *Wind* spacecraft. One detector (S1) points toward the south ecliptic pole, thereby observing the south ecliptic hemisphere; the other (S2) observes the north ecliptic hemisphere. Each detector has an effective area of $\sim 80\text{--}160 \text{ cm}^2$, depending on the photon energy and incident angle. In interplanetary space far outside the Earth's magnetosphere, KW has the advantages over Earth-orbiting GRB monitors of continuous coverage, uninterrupted by Earth occultation, and a steady background, undistorted by passages through the Earth's trapped radiation, and subject only to occasional solar particle events.

The instrument has two operational modes: waiting and triggered. In the waiting mode, the count rates are recorded in three energy windows: G1, G2, and G3, with 2.944 s time resolution. The nominal boundaries of the energy windows are 13–50 keV (G1), 50–200 keV (G2), and 200–750 keV (G3). When the count rate in the G2 window exceeds a $\sim 9\sigma$ threshold above the background on one of two fixed timescales, 1 s or 140 ms, the instrument switches into the triggered

mode. In the triggered mode, the count rates in G1, G2, and G3 are recorded with time resolutions varying from 2 ms up to 256 ms. Spectral measurements are carried out, starting from the trigger time, in two overlapping energy intervals, PHA1 (13–760 keV) and PHA2 (160 keV–10 MeV), with 64 spectra being recorded for each interval over a 63-channel, pseudo-logarithmic, energy scale.

The detector energy scale is calibrated in flight using the 1460 keV line of ^{40}K and the 511 keV $e^+ e^-$ annihilation line in the multichannel spectra. The gain of the detectors has slowly decreased during the long period of operation. Accounting for the gain loss, the full KW spectral band in the waiting mode ($G1+G2+G3$) during 2005–2018 was \sim 20–1500 keV for S1 and \sim 17–1250 keV for S2; the G1, G2, and G3 energy bounds shifted accordingly. A more detailed discussion of the KW instrument can be found in Svinkin et al. (2016) and T17.

As of 2018 December, KW has triggered \sim 4800 times on a variety of transient events, including \sim 3050 GRBs. Thus KW has been triggering on \sim 130 GRBs per year. Additionally, the KW waiting mode data search (Kozlova et al. 2019) revealed \sim 2200 untriggered GRBs detected by KW and simultaneously by BATSE, BeppoSAX, *Swift*, and *Fermi* during the same time interval. The KW databases of short bursts along with their IPN localization maps, GRBs with z , SGRs, and SFs can be found at the KW web page¹.

2.2. *Swift*/BAT

The *Swift* mission, dedicated to GRB studies, was launched on 2004 November 20 (Gehrels et al. 2004). The *Swift* payload is comprised of three instruments which work in tandem to provide rapid identification and multi-wavelength follow-up of GRBs and their afterglows: the Burst Alert Telescope (BAT), the X-ray Telescope (XRT; Burrows et al. 2005) and the UV-Optical Telescope (UVOT; Roming et al. 2005). When the BAT detects a GRB, *Swift* slews to the GRB position and observes the burst with the XRT and the UVOT, which can further refine the localization to \lesssim arcsec.

The BAT is a highly sensitive, large field of view (FoV: 1.4 sr for $>$ 50% coded FoV and 2.2 sr for $>$ 10% coded FoV), coded-aperture telescope that detects and localizes GRBs in real time. The BAT is composed of a detector plane that has 32,768 CdZnTe (CZT) detectors, and a coded-aperture mask that has \sim 52,000 lead tiles. The BAT energy range is 14–150 keV for imaging, which is a technique to subtract the background based on the modulation resulting from the coded mask; spectra with no position information can be obtained up to 350 keV. Details of the BAT instruments, including the in-orbit calibrations, can be found in Barthelmy et al. (2005) and the BAT GRB catalogs (Sakamoto et al. 2008, 2011a; Lien et al. 2016).

The sophisticated on-board localization capability of the BAT and the fast spacecraft pointing

¹<http://www.ioffe.ru/LEA/>

of *Swift* allow X-ray (optical) afterglow observations from the XRT (UVOT) within a few hundred seconds after the trigger for more than 90% (30%) of *Swift* GRBs (Sakamoto et al. 2008). The precise and rapid GRB location provided by *Swift* permits coordinated multi-wavelength observations on the ground that, in turn, provide a new opportunity to measure GRB redshifts and to use GRBs as cosmological probes.

3. The Burst Sample

The joint sample of the KW (waiting mode) and BAT bursts with known redshifts (hereafter, WM sample) was formed as follows. First, we extracted a set of BAT GRBs with known redshifts from the online *Swift* GRB Table² and excluded the bursts detected by KW in the triggered mode. Then we checked the reliability of the redshifts: we included only the bursts with z measured from the emission lines, the absorption features of the host galaxies imposed on the afterglow continuum, or photometrically.

The remaining set comprised \sim 300 bursts, for which, using a Bayesian block (BB) analysis (Scargle et al. 2013), we performed a targeted search for detections in the continuous KW waiting mode data. The decomposition of KW light curves in the G1+G2, G2, and G1+G2+G3 bands into BBs was performed on the 2.944 s time scale, using a custom tool³. The BB algorithm was tuned, for each energy band, to find intervals with $\gtrsim 4\sigma$ count rate excess over background (see, e.g. Kozlova et al. 2019 for more details). The presence of such interval(s), temporally coincident with the BAT trigger⁴, indicated a joint KW and BAT detection. Using this criterion, we found 203 joint KW and BAT GRB detections and about a dozen events with lower KW signal significance ($\gtrsim 3.2\sigma$), which were selected for the subsequent analysis manually. Two examples of joint KW+BAT detections, GRB 090429B ($z=9.38$) and GRB 110205A ($z=2.22$), are shown in Figure 2.

Finally, we performed joint spectral fits to the 3-channel KW waiting mode spectra, covering the \sim 20–1500 keV band, and the BAT spectra in the 15–150 keV band (see Section 4 for details), and selected only the bursts appropriately fitted with a “curved” spectral model (CPL or BAND) that allows E_p to be constrained. The final WM sample comprises 167 GRBs with reliable redshift estimates and constrained peak energies detected simultaneously by *Swift*/BAT and by KW in the waiting mode from the beginning of the *Swift* era in 2004 to the end of 2018. Four bursts from this sample are short ones (GRB 050724, GRB 060801, GRB 090426, and GRB 131004A) and three bursts are X-ray flashes (XRFs: GRB 080515, GRB 091018, and GRB 120922A). The general information about these bursts is presented in Table 1. The first three columns contain the GRB

²https://swift.gsfc.nasa.gov/archive/grb_table/

³https://github.com/dsvinkin/b_blocks

⁴The KW data timing was corrected for the light propagation time between *Wind* and *Swift* for the specific burst.

name as reported in the Gamma-ray Burst Coordinates Network circulars⁵, the BAT trigger ID and the BAT trigger time T_0 . The next three columns provide the burst redshift and information on it. For a number of GRBs there are several independent redshift estimates available, of which we gave a preference to spectroscopic over photometric redshift, if available; also, results from refereed papers, which presented a detailed spectral analysis, were given higher priority over earlier GCN circulars. The rightmost two columns of Table 1 contain the burst durations T_{100} along with t_0 , their start times relative to the BAT trigger time, determined using the BB decomposition of the BAT light curve in the 25–350 keV band. This energy band was selected as, first, being common between both instruments and, second, being less sensitive to weak precursors or soft extended tails (T17). More details on the T_{100} computation are given in Section 4.1.

The redshifts of GRBs in the WM sample span the range $0.04 \leq z \leq 9.4$ and have mean and median values of ~ 2.4 and ~ 2.2 , respectively. These statistics are comparable with those for the *Swift* era ($\bar{z} \sim 2.3$, Coward et al. 2013) but differ significantly from the statistics for the KW triggered bursts presented in T17, which were comparable with the pre-*Swift* era ones (Berger et al. 2005b). Figure 1 shows the redshift distributions for KW GRBs and all GRB redshifts available up to the end of 2018⁶.

4. Data Analysis and Results

4.1. Energy Spectra

We began the analysis with extraction of *Swift*/BAT spectral data and light curves, performing the following steps. First, we downloaded the data from the *Swift*/BAT Enhanced GRB Data Product Catalog⁷. These folders contain the results from Lien et al. (2016) obtained with BATGRBPROMPT, a standard automatic pipeline script for GRB processing, and some additional products required for the quick-look page. The detailed description of the data processing procedure may be found in the abovementioned paper. Then we constructed BAT light curves in the 25–350 keV range using a standard tool BATBINEVT from the software package HEASOFT. After that we did a BB decomposition of the BAT light curve using the BATBLOCKS task.

Based on the BB decomposition of BAT (25–350 keV) and KW (G1+G2, \sim 20–350 keV) light curves, we selected time intervals for spectral analysis. For each burst in our sample, two time intervals were selected: time-averaged fits were performed over the interval closest to T_{100} (hereafter the TI spectrum); the peak spectrum corresponds to the KW BB where the peak count

⁵http://gcn.gsfc.nasa.gov/gcn3_archive.html

⁶Gamma-Ray Burst Online Index: <http://www.astro.caltech.edu/grbox/grbox.php>

⁷https://swift.gsfc.nasa.gov/results/batgrbcatalog/<GRB_name>/data_product/<trigger_ID>-results-detection-mask (if it exists) or https://swift.gsfc.nasa.gov/results/batgrbcatalog/<GRB_name>/data_product/<trigger_ID>-results

rate (PCR) is reached. In some cases the T_{100} and the spectral interval boundaries were adjusted after visual inspection. The time interval between the beginning of the second BB and that of the last one was typically adopted as T_{100} .

Then we extracted BAT spectra for the selected intervals using the BATBINEVT tool and BATPHASYSERR task to include systematics. Since *Swift* slews at a rate of $\sim 1^\circ$ per second (Markwardt et al. 2007), the telescope motion should be taken into account if the spectrum accumulation time overlaps with the spacecraft slew time by more than 5 s. Thus, following Sakamoto et al. (2011a) (but see also Lien et al. 2016), we created an “average” response file for the whole spectrum from multiple 5-s response files using the HEASARC tool ADDRMRF with weighting factors equal to the fraction of light curve counts in the specific time periods of each response file. The 5-s response files were made with the BATDRMGEN tasks, and the spectral files were updated using the BATUPDATEPHAKW task.

We performed a joint spectral analysis of KW and BAT spectral data using XSPEC version 12.9.0 (Arnaud 1996) using the χ^2 statistic. Each spectrum was fitted by two spectral models, both normalized to the energy flux in the observer-frame 15 keV–1.5 MeV range. The first model is the Band function (hereafter BAND; Band et al. 1993):

$$f(E) \propto \begin{cases} E^\alpha \exp\left(-\frac{E(2+\alpha)}{E_p}\right), & E < (\alpha - \beta) \frac{E_p}{2+\alpha} \\ E^\beta \left[(\alpha - \beta) \frac{E_p}{(2+\alpha)}\right]^{(\alpha-\beta)} \exp(\beta - \alpha), & E \geq (\alpha - \beta) \frac{E_p}{2+\alpha}, \end{cases} \quad (1)$$

where α is the low-energy photon index and β is the high-energy photon index. The second spectral model is an exponentially cutoff power-law (CPL), parameterized as E_p :

$$f(E) \propto E^\alpha \exp\left(-\frac{E(2 + \alpha)}{E_p}\right). \quad (2)$$

The fits were performed in the energy range from ~ 15 keV to ~ 1.5 MeV. When fitting the BAT spectral data, channels 1–3 ($\lesssim 14$ keV) and the channels starting from 63 ($\gtrsim 149$ keV) were ignored. The parameter errors were estimated using the XSPEC command ERROR based on the change in fit statistic ($\Delta\chi^2 = 1$) which corresponds to the 68% confidence level (CL). The models were multiplied by a constant normalization factor to take into account the systematic effective area uncertainties in the response matrices of each instrument. The normalization factor of the KW data was fixed to unity, and the normalization factor of the BAT spectra was the free parameter. The latter, for our sample, is distributed approximately normally with mean ≈ 0.80 and $\sigma \approx 0.11$, in general agreement with the conclusion of Sakamoto et al. (2011b) that the intrinsic effective area of the BAT energy response file is 10%–20% smaller than that of the KW.

Examples of joint KW+BAT spectral fits for TI spectra of GRB 090429B and GRB 110205A are given in Figure 2. The results of the spectral analysis of the WM sample are presented in Table 2. For each spectrum, we present the results for the models whose parameters are constrained (hereafter, GOOD models). The spectral fits with the BAND model with $\beta < -3.5$, which are

typically poorly constrained, were excluded. The ten columns in Table 2 contain the following information: (1) the GRB name (see Table 1); (2) the spectrum type, where “i” indicates that the spectrum is time-integrated (TI), “p” means that the spectrum is peak (for some bursts with poor count statistics, the TI and the peak spectra are measured over the same interval); (3) and (4) contain the spectrum start time t_{start} (relative to T_0) and its accumulation time ΔT ; (5) GOOD models for each spectrum; (6)–(8) α , β , and E_p ; (9) F (normalization flux); (10) $\chi^2/\text{d.o.f.}$ along with the null hypothesis probability given in brackets. In cases where the lower limit for β is not constrained, the value of $(\beta_{\min} - \beta)$ is provided instead, where $\beta_{\min} = -10$ is the lower limit for the fits.

We found BAND to be a GOOD model for 56 TI and 50 peak spectra. The remaining spectra were well-fitted only by the CPL function. Table 3 summarizes the descriptive statistics for spectral parameters and energetics for the WM sample from this paper and the whole sample of KW GRBs with known redshifts. E_p varies from ≈ 27 keV to ≈ 580 keV for the WM sample and lies within a significantly wider range, from ≈ 27 keV to ≈ 3.7 MeV, for the whole KW sample. The TI spectrum E_p ($E_{p,i}$) has its median value at 111 keV, while the peak spectrum E_p ($E_{p,p}$) median value is 136 keV. The rest-frame peak energies of the whole KW sample, $E_{p,i,z} = (1+z)E_{p,i}$ and $E_{p,p,z} = (1+z)E_{p,p}$, cover a wide range from ≈ 53 keV to ≈ 7 MeV (GRB 090510).

4.2. Burst Energetics

The energy fluences (S) and the peak energy fluxes (F_{peak}) were derived using the 15 keV–1.5 MeV normalization fluxes from the spectral fits with the BAND model (or the CPL function if the fit with the BAND model was not constrained) for TI and peak spectra, respectively. Since the TI spectrum accumulation interval may differ from the T_{100} interval, a correction which accounts for the emission outside the TI spectrum was introduced when calculating S . Following T17 three time scales ΔT_{peak} were used when calculating F_{peak} : 1 s, 64 ms, and the “rest-frame 64 ms” scale $((1+z) \cdot 64 \text{ ms})$; the latter was used to estimate the rest-frame peak luminosity L_{iso} . To obtain F_{peak} , the model energy flux of the peak spectrum was multiplied by the ratio of the PCR on the ΔT_{peak} scale to the average count rate in the spectral accumulation interval. Both corrections were calculated using counts in the BAT light curve in the 25–350 keV band.

The cosmological rest-frame energetics, the isotropic-equivalent energy release E_{iso} and the isotropic-equivalent peak luminosity L_{iso} , can be calculated as $E_{\text{iso}} = \frac{4\pi D_L^2}{1+z} \times S \times k$ and $L_{\text{iso}} = 4\pi D_L^2 \times F_{\text{peak}} \times k$, with the proper k -correction, which transforms the energetics from the observer-frame 1.5 keV–1.5 MeV energy range to the $1/(1+z)$ keV–10 MeV band.

Knowing t_{jet} , one can estimate the collimation-corrected energy released in gamma-rays $E_\gamma = E_{\text{iso}}(1 - \cos \theta_{\text{jet}})$ and the collimation-corrected peak luminosity $L_\gamma = L_{\text{iso}}(1 - \cos \theta_{\text{jet}})$, where θ_{jet} is the jet opening angle and $(1 - \cos \theta_{\text{jet}})$ is the collimation factor. We consider two types of circumburst medium (CBM): a CBM with constant number density n , hereafter homogeneous

medium, or HM, and a stellar-wind-like CBM with $n(r) \propto r^{-2}$, hereafter SWM. In this work, we only use the jet breaks that were detected either in optical/IR afterglow light curves or in two spectral bands simultaneously. We found reasonably-constrained jet break times for 14 bursts in the literature (including one short GRB), and for six of them the HM was taken to be the most probable CBM. See T17 for further details on the calculation of jet opening angles.

Table 4 summarizes observer-frame and isotropic-equivalent rest-frame energetics. The first two columns are the GRB name and z . The next seven columns present the observer-frame energetics: S ; peak fluxes on the three time scales: $F_{\text{peak},1000}$ (1 s), $F_{\text{peak},64}$ (64 ms), and $F_{\text{peak},64,r}$ ($(1+z) \cdot 64$ ms); together with the start times of the intervals when the PCR is reached: $T_{\text{peak},1000}$, $T_{\text{peak},64}$, and $T_{\text{peak},64,r}$. The rightmost two columns contain E_{iso} and the peak isotropic luminosity, L_{iso} , calculated from $F_{\text{peak},64,r}$. These L_{iso} values may be adjusted to a different time scale ΔT (64 ms or 1 s) as:

$$L_{\text{iso}}(\Delta T) = \frac{F_{\text{peak}}(\Delta T)}{F_{\text{peak},64,r}} L_{\text{iso}}.$$

The most fluent burst in our sample is GRB 110205A ($S \approx 4.1 \times 10^{-5}$ erg cm $^{-2}$). The brightest burst based on the peak energy flux is GRB 050724 ($F_{\text{peak},64,r} \approx 2.9 \times 10^{-6}$ erg cm $^{-2}$ s $^{-1}$). The most energetic burst in terms of the isotropic energy is GRB 050904 ($E_{\text{iso}} \approx 1.4 \times 10^{54}$ erg). The most luminous burst is GRB 130606A ($L_{\text{iso}} = 3.6 \times 10^{53}$ erg s $^{-1}$).

The collimation-corrected energetics for 14 bursts with “reliable” jet break times is presented in Table 5. The first column is the burst name. The next three columns specify t_{jet} , the CBM environment implied, and references to them. The next columns contain the derived jet opening angles and the corresponding collimation factors, and the last two columns present E_{γ} and L_{γ} . For bursts with no reasonable constraint on the CBM profile the results are given for both HM and SWM. The HM jet opening angles vary from 1.3° to 10.2° and the corresponding collimation factors from 0.0002 to 0.016. The brightest burst in terms of both E_{γ} and L_{γ} is GRB 060418 ($E_{\gamma,\text{HM}} \simeq 2.3 \times 10^{51}$ erg, $L_{\gamma,\text{HM}} \simeq 2.9 \times 10^{50}$ erg s $^{-1}$, $\theta_{\text{jet,HM}} \simeq 10.0^\circ$).

4.3. Comparison with T17 Results

Concluding the WM sample analysis, we note some differences between the results obtained in this work and the ones for the sample of triggered KW bursts (T17). The first is a bias towards fainter and spectrally-softer GRBs in this catalog that comes from different detection algorithms. The KW hardware trigger operates at 9σ threshold in the ~ 80 – 350 keV band and strongly suppresses the detection of bursts with $E_p \lesssim 100$ keV (Section 5.3 in T17). Accordingly, the T17 sample is comprised of relatively bright and spectrally-hard GRBs, with the median E_p of ~ 240 keV and $F_{\text{peak}} \gtrsim 1 \times 10^{-6}$ erg cm $^{-2}$ s $^{-1}$. The KW WM sample, that excludes the triggered events, was formed through a targeted search of BAT GRBs in the continuous KW waiting-mode data (Section 3). The search was performed in several KW energy bands, starting from ~ 20 keV, with an effective detection threshold in each band of $\sim 4\sigma$. As a result, the median E_p in the WM sample

(~ 115 keV) is a factor of two lower than that of T17 (Figure 3); the brightest WM burst has F_{peak} just a few times higher than the T17 lower limit, $\sim 3 \times 10^{-6}$ erg cm $^{-2}$ s $^{-1}$, while the weakest one has $F_{\text{peak}} \sim 1 \times 10^{-7}$ erg cm $^{-2}$ s $^{-1}$. Thus, thanks to the high sensitivity of BAT, the sample-wide flux threshold has been reduced by an order of magnitude as compared to T17.

In T17, burst energetics were estimated using the flux of the BEST spectral model chosen based on the difference in χ^2 between the CPL and the BAND fits to KW multichannel spectra. The criterion for accepting the model with the single additional parameter was the change in χ^2 of at least 6 ($\Delta\chi^2 \equiv \chi^2_{\text{CPL}} - \chi^2_{\text{BAND}} > 6$). For the WM sample, the high-energy part of the analyzed spectrum (above 150 keV) is represented by just two wide KW waiting mode spectral channels, which, in many cases, allowed us to constrain the high-energy photon index β (and, simultaneously, better constrain E_p as compared to a CPL fit to the same spectrum). On the other hand, with the lack of detailed spectral coverage at the higher energies, our fits with the two models did not typically result in a statistically-significant $\Delta\chi^2$ between the BAND and CPL fits. Thus, in order not to underestimate the high-energy flux we calculated the burst energetics using the BAND model fit when it is constrained.

Atteia et al. (2017) and T17 found a good agreement between KW- and *Fermi*/GBM-derived energetics and spectra of several dozen commonly detected bright GRBs with known redshifts. The WM sample studied in this work contains 45 faint GRBs independently detected by *Fermi*/GBM. For ~ 30 GBM bursts with constrained peak energies, we compared the E_p of time-integrated spectra and fluences reported in the GBM catalog⁸ with those obtained in this work. In 27 cases where the KW+BAT and the GBM fits were made over comparable time intervals, we found them to agree within errors.

5. Discussion

5.1. The progress achieved with this catalog

This work extends the first part of the KW catalog of GRBs with known redshifts (T17) which provided temporal and spectral parameters, as well as broadband observer- and rest-frame energetics of 150 bursts detected in the KW triggered mode in a wide ~ 20 keV–20 MeV energy range, with the sample-wide peak flux limit of $\sim 1 \times 10^{-6}$ erg cm $^{-2}$ s $^{-1}$. Extended up to the end of 2018, this sample comprises 171 GRBs with $0.1 \leq z \leq 5$.

With 167 GRBs from the WM sample added, the total number of KW bursts with known redshifts increases to 338 GRBs, the largest set of cosmological GRBs studied to date over a broad energy band. It includes 43 long bursts with reliable t_{jet} estimates, and 14 short/hard “type I” GRBs. With the flux limit of $F_{\text{peak}} \sim 1 \times 10^{-7}$ erg cm $^{-2}$ s $^{-1}$ (Figure 5), the KW sample spans

⁸<https://heasarc.gsfc.nasa.gov/W3Browse/fermi/fermigrbst.html>

redshifts $0.04 \leq z \leq 9.4$, isotropic luminosities L_{iso} from $\sim 2 \times 10^{48} \text{ erg s}^{-1}$ to $\sim 5 \times 10^{54} \text{ erg s}^{-1}$, isotropic energies E_{iso} from $\sim 3 \times 10^{49} \text{ erg}$ to $\sim 6 \times 10^{54} \text{ erg}$, and intrinsic peak energies from $\sim 50 \text{ keV}$ to $\sim 7 \text{ MeV}$. At this time, we do not include six KW ultra-long (with durations $>1000 \text{ s}$) GRBs with known redshifts in this sample; their properties will be reported elsewhere.

5.2. Hardness-Intensity Correlations

The large set of measured GRB redshifts, together with well-determined prompt emission spectra and fluences, can provide an excellent testing ground for the widely discussed correlations between rest-frame spectral hardness and energetics, e.g., the “Amati” (Amati et al. 2002), “Yonetoku” (Yonetoku et al. 2004) or “Ghirlanda” (Ghirlanda et al. 2007) relations. This could facilitate using GRBs as standard candles (see, e.g., Atteia 1997 or Friedman & Bloom 2005) and probing cosmological parameters with GRBs (see, e.g., Cohen & Piran 1997 or Diaferio et al. 2011).

Using the updated KW sample, and following the methodology of T17, we tested the rest-frame Amati ($E_{\text{p,i,z}} - E_{\text{iso}}$) and Yonetoku ($E_{\text{p,p,z}} - L_{\text{iso}}$) correlations, along with their collimated versions, $E_{\text{p,i,z}} - E_{\gamma}$ and $E_{\text{p,p,z}} - L_{\gamma}$. To probe the existence of correlations, we calculated the Spearman rank-order correlation coefficients (ρ_S) and the associated null-hypothesis (chance) probabilities or p-values (P_{ρ_S} ; Press et al. 1992). We approximated linear regression between log-energy and $\log - E_{\text{p}}$ using two methods, with and without intrinsic scatter (σ_{int}). The fit was performed using the MPFITEXY routine⁹ (Williams et al. 2010), which depends on the MPFIT package (Markwardt 2009).

The correlation parameters obtained for the subsample of 316 long (or type II) GRBs, and 43 long bursts with t_{jet} estimates are summarized in Table 6. The first column presents the correlation. The next three columns provide the number of bursts in the fit sample, ρ_S , and P_{ρ_S} . The next columns specify the slopes (a), the intercepts (b), and σ_{int} . The derived slopes of the Amati and Yonetoku relations are very close to each other, 0.429 ($\rho_S=0.70$, 316 GRBs) and 0.428 ($\rho_S=0.70$, 316 GRBs), respectively. When accounting for the intrinsic scatter, these slopes change to a more gentle ~ 0.31 (with $\sigma_{\text{int}} \sim 0.23$). It should be noted that the slopes of both correlations for the extended GRB sample are slightly shallower than those for the sample from T17. Figure 4 represents the correlations for the long (type II) GRBs from the KW sample.

The subsample of GRBs with reliable t_{jet} estimates comprises 43 long bursts. The Ghirlanda relations were tested against the Amati and Yonetoku relations for the same subset of GRBs. The geometric mean of the HM and SWM collimation factors was used for the bursts with unknown CBM. With the whole KW sample we confirm the result of T17 that accounting for the jet collimation neither improves the significance of the correlations nor reduces the dispersion of the points around the best-fit relations. The slopes we obtained for the collimated Amati and Yonetoku

⁹<http://purl.org/mike/mpfitexy>

relations are steeper compared to those of the non-collimated versions.

5.3. GRB Luminosity and Isotropic-energy Functions, and GRB Formation Rate

With the updated sample of 315 long KW GRBs with known z , we estimated the luminosity function (LF; the number of bursts per unit luminosity), the isotropic energy release function (EF; the number of bursts per unit energy release), and the cosmic GRB formation rate (GRBFR; the number of events per comoving volume and time). Our approach (details are given in T17) relies on the non-parametric Lynden-Bell C[−] technique (Lynden-Bell 1971) further advanced by Efron & Petrosian (1992) (LBEP method).

Without loss of generality, the total LF $\Phi(L_{\text{iso}}, z)$ ¹⁰ can be rewritten as $\Phi(L_{\text{iso}}, z) = \rho(z)\phi(L_{\text{iso}}/g(z), \zeta)/g(z)$, where $\rho(z)$ is the GRB formation rate (GRBFR); $\phi(L_{\text{iso}}/g(z))$ is the local LF; $g(z)$ is the luminosity evolution that parameterizes the correlation between L and z ; and ζ stands for the cosmological evolution of the LF shape parameters, whose effect is commonly ignored as the shape of the LF does not change significantly with z (e.g. Yonetoku et al. 2004).

Following Lloyd-Ronning et al. (2002), Yonetoku et al. (2004), Wu et al. (2012), and Yu et al. (2015) we chose the functional form $g(z) = (1+z)^{\delta}$ for the luminosity evolution. It should be noted that the isotropic luminosity evolution can be determined by either the evolution of the amount of energy per unit time emitted by the GRB progenitor or by the jet opening angle evolution (see, e.g., Lloyd-Ronning et al. (2002) for the discussion); we tested the KW sample for a correlation between the collimation factor and $1+z$ and, as in T17, found the correlation negligible (the Spearman rank-order correlation coefficient $\rho_S \approx -0.4$, and the corresponding p -value $P_{\rho_S} \approx 0.01$) for the subsample of 43 long (or type II) bursts with known collimation factors. See T17 (Section 5.5 and Appendix) for further details on the non-parametric method used for the calculations.

Since the LBEP method was specifically designed to reconstruct the intrinsic distributions from the observed distributions, takes into account the data truncations introduced by observational bias, and includes the effects of the possible correlation between the two variables, the correct estimation of the threshold fluxes and fluences plays a crucial role in the application of this technique. The first panel of Figure 5 shows the distribution of KW bursts in the $L_{\text{iso}}-z$ diagram. The blue dashed line corresponds to the truncation flux $F_{\text{lim}} \sim 2.0 \times 10^{-6} \text{ erg cm}^{-2} \text{ s}^{-1}$ for the triggered sample of type II GRBs from T17, while the solid line represents the truncation flux $F_{\text{lim}} \sim 1.7 \times 10^{-7} \text{ erg cm}^{-2} \text{ s}^{-1}$ for the joint sample of waiting mode and triggered KW GRBs. The threshold fluence used for the EF estimates is $S_{\text{lim}} \sim 1.6 \times 10^{-6} \text{ erg cm}^{-2}$.

Applying the LBEP method to the $z-L_{\text{iso}}$ plane for the long (type II) bursts from the joint sample of KW GRBs with z , we found that the independence of the variables is rejected at $\sim 1.8\sigma$,

¹⁰Similar reasoning may be applied to the total EF $\Psi(E_{\text{iso}}, z)$

and the best luminosity evolution index is $\delta_L = 1.2_{-0.6}^{+0.6}$. Applying the same method to the z - E_{iso} plane of the same sample we found that the independence of the variables is rejected at $\sim 1.8\sigma$, and the best isotropic energy evolution index is $\delta_E = 1.1_{-0.6}^{+1.0}$. Note that the estimated E_{iso} and L_{iso} evolutions are comparable. The evolution PL indices δ_L and δ_E derived here are shallower than those reported in the previous studies: $\delta_L = 2.60_{-0.20}^{+0.15}$ (Yonetoku et al. 2004), $\delta_L = 2.30_{-0.51}^{+0.56}$ (Wu et al. 2012), $\delta_L = 2.43_{-0.38}^{+0.41}$ (Yu et al. 2015), and $\delta_E = 1.80_{-0.63}^{+0.36}$ (Wu et al. 2012), and comparable with the indices from T17 ($\delta_L = 1.7_{-0.9}^{+0.9}$, $\delta_E = 1.1_{-0.7}^{+1.5}$).

The luminosity and energy release evolution can be eliminated dividing by $g(z)$: $L' = L_{\text{iso}}/(1+z)^{\delta_L}$ and $E' = E_{\text{iso}}/(1+z)^{\delta_E}$, where L' and E' are the local luminosity and energy release, correspondingly. Then the cumulative distributions¹¹ $\psi(L)$, $\psi(L')$, $\psi(E)$, and $\psi(E')$ were fitted with a broken power-law (BPL) function:

$$\psi(x) \propto \begin{cases} x^{\alpha_1}, & x \leq x_b, \\ x_b^{(\alpha_1-\alpha_2)} x^{\alpha_2}, & x > x_b, \end{cases}$$

where α_1 and α_2 are the PL indices of the dim and bright distribution segments, and x_b is the breakpoint of the distribution; and with the CPL function¹²: $\psi(x) \propto x^\alpha \exp(-x/x_{\text{cut}})$, where x_{cut} is the cutoff luminosity (or energy).

The fits were performed in log–log space; the results are given in Table 7 and shown in Figure 5 (bottom panels). In Table 7 the central values of parameters are the best-fit values derived for the original data sets, and the upper and lower uncertainties are calculated from the 68% quantiles computed for 10000 bootstrapped samples. The derived BPL slopes of the LF and EF are close to each other, both for the dim and bright segments, so the shape of the EF is similar to that of the LF. The BPL indices derived for the LF are in agreement with those obtained in Yonetoku et al. (2004) ($\alpha_1 = -0.29 \pm 0.02$ and $\alpha_2 = -1.02 \pm 0.02$), while the indices computed in Yu et al. (2015) are shallower ($\alpha_1 = -0.14 \pm 0.02$ and $\alpha_2 = -0.70 \pm 0.03$); the BPL indices derived for the EF are marginally consistent with those obtained in Wu et al. (2012) ($\alpha_1 = -0.27 \pm 0.01$ and $\alpha_2 = -0.87 \pm 0.07$). Using the bootstrap approach we found that BPL better fits the $\psi(L)$ for $\sim 95\%$ of the datasets, while CPL better fits the $\psi(E)$ for $\sim 70\%$ of bootstrapped sets. The existence of a sharp cutoff of the isotropic energy distribution of KW and *Fermi*/GBM GRBs around $\sim 1 - 3 \times 10^{54}$ erg was suggested by Atteia et al. (2017) and confirmed by T17.

We estimated the cumulative GRB number distribution $\psi(z)$ and the derived GRBF per unit time per unit comoving volume $\rho(z)$ using the LBEP method. In Panel B of Figure 5 we compare the star formation rate (SFR) data from the literature with GRBFs derived from different z - L and z - E distributions. The GRBF estimated from all distributions (both corrected and uncorrected for the cosmological evolution of energetics) shows a relative excess over the SFR at $z < 1$ and

¹¹ $\phi(x) = -d\psi(x)/dx$

¹²The CPL function definition is different here from that in Section 4.1

nearly traces the SFR at higher redshifts. The low- z GRBFR excess over SFR was reported in Yu et al. (2015), Petrosian et al. (2015) and T17; this work confirms those findings at a higher significance.

We performed simulations to test whether this relative excess of the GRBFR over the SFR is an artefact of the LBEP method. First, we generated a set of 300 (z, L_{iso}) pairs, with $L_{\text{iso}} \gtrsim 10^{47} \text{ erg s}^{-1}$ that follow the cumulative distribution $\psi(L)$ estimated above; a redshift distribution following the SFR approximation (Li 2008); and the sample truncating flux $F_{\text{lim}} = 1.7 \times 10^{-7} \text{ erg cm}^{-2} \text{ s}^{-1}$, similar to that for the KW sample. Then, the cosmological evolution $g(z)$ with $\delta_L = 1.2$ (as estimated above) was applied to the simulated luminosities and the final set of (z, L') pairs was generated from (z, L) . We processed the simulated (z, L') sample using the LBEP methodology described above and obtained a $\rho(z)$ that perfectly traces the seed SFR in the whole range of simulated redshifts $0.01 \lesssim z \lesssim 10$. The simulations were repeated several times with similar results. Thus, the implied low- z GRBFR excess cannot be attributed to our analysis and may be intrinsic.

One of the possible keys to explain this relative excess of GRBFR over SFR may be the preference of long GRBs for low-mass galaxies and low-metallicity environments which are not unbiased tracers of the star formation rate at low redshifts (see, e.g., Lloyd-Ronning et al. 2019 and references therein for further discussion). Another reason may be the presence of selection effects based on the incompleteness of the sample: it is easier to measure the redshifts of nearest GRBs thereby creating a bias towards them which, in turn, will lead to the relative excess of low- z bursts over the rest of the unbiased sample (see Pescalli et al. 2016). The “external” selection effects (i.e. not related to the prompt emission), arising from the complex procedure of redshift measurements, are very important but extremely hard to estimate (see, however, Petrosian et al. (2015) who made an attempt to estimate the selection effect in X-rays). At least three biases may contribute to this: the ability to localize the GRB precisely, the ability of optical/NIR telescopes to start following the afterglow rapidly, and the factors affecting the detectability of spectral lines in the afterglow spectra. Although the “external” biases are very important, their investigation lies beyond the scope of this paper.

6. Summary and Conclusions

We have presented the results of a systematic study of GRBs with reliable redshift estimates simultaneously detected in the waiting mode of the Konus-*Wind* experiment and in the triggered mode of the *Swift/BAT* experiment. The sample covers the period from 2005 January to 2018 December. By taking advantage of the high sensitivity of *Swift/BAT* and the wide spectral band of KW we were able to constrain the peak spectral energies, the broadband energy fluences, and the peak fluxes for the joint KW-BAT sample of 167 weak ($F_{\text{peak}} \lesssim 3 \times 10^{-6} \text{ erg cm}^{-2} \text{ s}^{-1}$), relatively soft GRBs (including four short bursts). From the spectral analyses of the sample, we provide the spectral fits with CPL and Band model functions. We calculated the 10 keV–10 MeV energy

fluences and the peak energy fluxes on three time scales, including the GRB rest-frame 64 ms scale. Based on the GRB redshifts, we estimated the rest-frame, isotropic-equivalent energies (E_{iso}) and peak luminosities (L_{iso}). For 14 GRBs with reasonably constrained jet breaks we provide the collimation-corrected values of the energetics.

This work extends the sample of KW bursts with known redshifts to 338 GRBs, the largest set of cosmological GRBs studied to date over a broad energy band. With the sample-wide flux limit of $F_{\text{peak}} \sim 1 \times 10^{-7} \text{ erg cm}^{-2} \text{ s}^{-1}$, it spans redshifts $0.04 \leq z \leq 9.4$, bolometric isotropic luminosities L_{iso} from $\sim 2 \times 10^{48} \text{ erg s}^{-1}$ to $\sim 5 \times 10^{54} \text{ erg s}^{-1}$, and isotropic energies E_{iso} from $\sim 3 \times 10^{49} \text{ erg}$ to $\sim 6 \times 10^{54} \text{ erg}$; and intrinsic peak energies from $\sim 50 \text{ keV}$ to $\sim 7 \text{ MeV}$.

Accounting for instrumental bias and using non-parametric techniques, we estimated the GRB luminosity evolution, luminosity and isotropic-energy functions, and the evolution of the GRB formation rate for the whole sample of 316 long KW GRBs with known redshifts. The derived luminosity evolution and isotropic energy evolution indices $\delta_L \sim 1.2$ and $\delta_E \sim 1.1$ are more shallow than those reported in previous studies and are in agreement with T17. The shape of the derived LF is best described by a broken PL function with low- and high-luminosity slopes ~ -0.3 and ~ -1 , respectively. The EF is better described by an exponentially cut off PL with the PL index ~ -0.3 and a cutoff isotropic energy $\sim 10^{54} \text{ erg}$. The derived GRBFR nearly traces the SFR at $z \gtrsim 1$. At $z < 1$, however, it features an excess over the SFR, that cannot be attributed to an analysis artefact. Finally, we considered the behavior of the rest-frame GRB parameters in the hardness-intensity planes, and confirmed the “Amati” and “Yonetoku” relations for long GRBs. We confirm the result of T17 that the correction for the jet collimation does not improve these correlations for this sample.

Plots of the GRB light curves and spectral fits can be found at the Ioffe Web site¹³. We hope this catalog will encourage further investigations of GRB physical properties and will contribute to other related studies.

We thank the anonymous referee for helpful comments on the manuscript. We gratefully thank Takanori Sakamoto and Amy Yarleen Lien for helpful discussions on BAT data processing and for their useful comments on the manuscript. We acknowledge a stimulating discussion with Valentin Pal’shin during an early stage of this work. We thank Vahé Petrosian and Maria Giovanna Dainotti for the enlightening conversations on the LBEP technique. We acknowledge the use of the public data from the *Swift* data archive¹⁴ and the Gamma-Ray Burst Online Index (“GRBOX”)¹⁵.

Facility: *Wind*(Konus), *Swift*(BAT)

¹³<http://www.ioffe.ru/LEA/zGRBs/part2/>

¹⁴<http://swift.gsfc.nasa.gov>

¹⁵<http://www.astro.caltech.edu/grbox/grbox.php>

REFERENCES

- Abdo, A. A., Ackermann, M., Arimoto, M., et al. 2009, Science, 323, 1688, doi: [10.1126/science.1169101](https://doi.org/10.1126/science.1169101)
- Afonso, P., Greiner, J., Pian, E., et al. 2011, A&A, 526, A154, doi: [10.1051/0004-6361/200913965](https://doi.org/10.1051/0004-6361/200913965)
- Amati, L., Frontera, F., Tavani, M., et al. 2002, A&A, 390, 81
- Aptekar, R. L., Frederiks, D. D., Golenetskii, S. V., et al. 1995, Space Sci. Rev., 71, 265, doi: [10.1007/BF00751332](https://doi.org/10.1007/BF00751332)
- Arnaud, K. A. 1996, in Astronomical Society of the Pacific Conference Series, Vol. 101, Astronomical Data Analysis Software and Systems V, ed. G. H. Jacoby & J. Barnes, 17
- Atteia, J.-L. 1997, A&A, 328, L21
- Atteia, J.-L., Heussaff, V., Dezelay, J.-P., et al. 2017, ApJ, 837, 119, doi: [10.3847/1538-4357/aa5ffa](https://doi.org/10.3847/1538-4357/aa5ffa)
- Band, D., Matteson, J., Ford, L., et al. 1993, ApJ, 413, 281, doi: [10.1086/172995](https://doi.org/10.1086/172995)
- Barthelmy, S. D., Barbier, L. M., Cummings, J. R., et al. 2005, Space Sci. Rev., 120, 143, doi: [10.1007/s11214-005-5096-3](https://doi.org/10.1007/s11214-005-5096-3)
- Berger, E., Cenko, S. B., Steidel, C., Reddy, N., & Fox, D. B. 2005a, GCN Circ. 3368. <http://gcn.gsfc.nasa.gov/gcn/gcn3/3368.gcn3>
- Berger, E., Foley, R., Simcoe, R., & Irwin, J. 2008, GCN Circ. 8434. <http://gcn.gsfc.nasa.gov/gcn/gcn3/8434.gcn3>
- Berger, E., Fox, D. B., & Cucchiara, A. 2007a, GCN Circ. 6470. <http://gcn.gsfc.nasa.gov/gcn/gcn3/6470.gcn3>
- Berger, E., Kulkarni, S. R., Fox, D. B., et al. 2005b, ApJ, 634, 501, doi: [10.1086/491667](https://doi.org/10.1086/491667)
- Berger, E., Fox, D. B., Kulkarni, S. R., et al. 2005c, ApJ, 629, 328, doi: [10.1086/431579](https://doi.org/10.1086/431579)
- Berger, E., Fox, D. B., Price, P. A., et al. 2007b, ApJ, 664, 1000, doi: [10.1086/518762](https://doi.org/10.1086/518762)
- Bloom, J. S., Perley, D., Foley, R., et al. 2005, GCN Circ. 3758. <http://gcn.gsfc.nasa.gov/gcn/gcn3/3758.gcn3>
- Bolmer, J., Graham, J., Knust, F., & Greiner, J. 2015a, GCN Circ. 18598. <http://gcn.gsfc.nasa.gov/gcn/gcn3/18598.gcn3>
- Bolmer, J., Knust, F., & Greiner, J. 2015b, GCN Circ. 18603. <http://gcn.gsfc.nasa.gov/gcn/gcn3/18603.gcn3>

- Bouwens, R. J., Illingworth, G. D., Labbe, I., et al. 2011, Nature, 469, 504, doi: 10.1038/nature09717
- Burrows, D. N., Hill, J. E., Nousek, J. A., et al. 2005, Space Sci. Rev., 120, 165, doi: 10.1007/s11214-005-5097-2
- Cabrera Lavers, A., de Ugarte Postigo, A., Castro-Tirado, A. J., et al. 2011, GCN Circ. 12234. <http://gcn.gsfc.nasa.gov/gcn/gcn3/12234.gcn3>
- Castro-Tirado, A. J., Gorosabel, J., & Garcia-Rodriguez, A. 2014a, GCN Circ. 16797. <http://gcn.gsfc.nasa.gov/gcn/gcn3/16797.gcn3>
- Castro-Tirado, A. J., Sanchez-Ramirez, R., Gorosabel, J., et al. 2013, GCN Circ. 14796. <http://gcn.gsfc.nasa.gov/gcn/gcn3/14796.gcn3>
- Castro-Tirado, A. J., Cunniffe, R., Sanchez-Ramirez, R., et al. 2014b, GCN Circ. 16505. <http://gcn.gsfc.nasa.gov/gcn/gcn3/16505.gcn3>
- Castro-Tirado, A. J., Valeev, A. F., Sokolov, V. V., et al. 2016, GCN Circ. 20077. <http://gcn.gsfc.nasa.gov/gcn/gcn3/20077.gcn3>
- Cenko, S. B., Fox, D. B., Cucchiara, A., et al. 2007, GCN Circ. 6556. <http://gcn.gsfc.nasa.gov/gcn/gcn3/6556.gcn3>
- Cenko, S. B., Hora, J. L., & Bloom, J. S. 2011, GCN Circ. 11638. <http://gcn.gsfc.nasa.gov/gcn/gcn3/11638.gcn3>
- Cenko, S. B., Levan, A. J., & Cucchiara, A. 2013, GCN Circ. 14762. <http://gcn.gsfc.nasa.gov/gcn/gcn3/14762.gcn3>
- Chary, R., Berger, E., & Cowie, L. 2007, ApJ, 671, 272, doi: 10.1086/522692
- Chen, H.-W., Helsby, J., Shectman, S., Thompson, I., & Crane, J. 2009, GCN Circ. 10038. <http://gcn.gsfc.nasa.gov/gcn/gcn3/10038.gcn3>
- Chornock, R., Berger, E., & Fox, D. 2011a, GCN Circ. 12537. <http://gcn.gsfc.nasa.gov/gcn/gcn3/12537.gcn3>
- Chornock, R., Berger, E., Fox, D., et al. 2010, GCN Circ. 11164. <http://gcn.gsfc.nasa.gov/gcn/gcn3/11164.gcn3>
- Chornock, R., Berger, E., & Fox, D. B. 2011b, GCN Circ. 11538. <http://gcn.gsfc.nasa.gov/gcn/gcn3/11538.gcn3>
- Chornock, R., Cenko, S. B., Griffith, C. V., et al. 2009a, GCN Circ. 9151. <http://gcn.gsfc.nasa.gov/gcn/gcn3/9151.gcn3>

- Chornock, R., Fox, D. B., Cucchiara, A., Perley, D. A., & Levan, A. 2014a, GCN Circ. 16301. <http://gcn.gsfc.nasa.gov/gcn/gcn3/16301.gcn3>
- Chornock, R., Fox, D. B., Tanvir, N. R., & Berger, E. 2014b, GCN Circ. 15966. <http://gcn.gsfc.nasa.gov/gcn/gcn3/15966.gcn3>
- Chornock, R., Lunnan, R., & Berger, E. 2013, GCN Circ. 15307. <http://gcn.gsfc.nasa.gov/gcn/gcn3/15307.gcn3>
- Chornock, R., Perley, D. A., & Cobb, B. E. 2009b, GCN Circ. 10100. <http://gcn.gsfc.nasa.gov/gcn/gcn3/10100.gcn3>
- Coward, D. M., Howell, E. J., Branchesi, M., et al. 2013, MNRAS, 432, 2141, doi: 10.1093/mnras/stt537
- Cucchiara, A., Bloom, J. S., & Cenko, S. B. 2011a, GCN Circ. 12202. <http://gcn.gsfc.nasa.gov/gcn/gcn3/12202.gcn3>
- Cucchiara, A., & Cenko, S. B. 2013, GCN Circ. 15624. <http://gcn.gsfc.nasa.gov/gcn/gcn3/15624.gcn3>
- Cucchiara, A., & Fox, D. B. 2008, GCN Circ. 7654. <http://gcn.gsfc.nasa.gov/gcn/gcn3/7654.gcn3>
- Cucchiara, A., Fox, D. B., Cenko, S. B., & Price, P. A. 2007, GCN Circ. 6083. <http://gcn.gsfc.nasa.gov/gcn/gcn3/6083.gcn3>
- Cucchiara, A., & Tanvir, N. R. 2012, GCN Circ. 13217. <http://gcn.gsfc.nasa.gov/gcn/gcn3/13217.gcn3>
- . 2013, GCN Circ. 14621. <http://gcn.gsfc.nasa.gov/gcn/gcn3/14621.gcn3>
- Cucchiara, A., Levan, A. J., Fox, D. B., et al. 2011b, ApJ, 736, 7, doi: 10.1088/0004-637X/736/1/7
- D’Avanzo, P., D’Elia, V., & Covino, S. 2008, GCN Circ. 8350. <http://gcn.gsfc.nasa.gov/gcn/gcn3/8350.gcn3>
- D’Avanzo, P., Sparre, M., Watson, D., et al. 2011, GCN Circ. 12284. <http://gcn.gsfc.nasa.gov/gcn/gcn3/12284.gcn3>
- de Ugarte Postigo, A., Cano, Z., Izzo, L., et al. 2018, GCN Circ. 22346, 1. <http://gcn.gsfc.nasa.gov/gcn/gcn3/22346.gcn3>
- de Ugarte Postigo, A., Gorosabel, J., Malesani, D., Fynbo, J. P. U., & Levan, A. J. 2009, GCN Circ. 9383. <http://gcn.gsfc.nasa.gov/gcn/gcn3/9383.gcn3>
- de Ugarte Postigo, A., Izzo, L., Kann, D. A., et al. 2017a, GCN Circ. 22272, 1. <http://gcn.gsfc.nasa.gov/gcn/gcn3/22272.gcn3>

- de Ugarte Postigo, A., Izzo, L., Thoene, C., et al. 2017b, GCN Circ. 20584. <http://gcn.gsfc.nasa.gov/gcn/gcn3/20584.gcn3>
- de Ugarte Postigo, A., Kruehler, T., Flores, H., & Fynbo, J. P. U. 2015, GCN Circ. 17523. <http://gcn.gsfc.nasa.gov/gcn/gcn3/17523.gcn3>
- de Ugarte Postigo, A., Tanvir, N., Sanchez-Ramirez, R., et al. 2013, GCN Circ. 14437. <http://gcn.gsfc.nasa.gov/gcn/gcn3/14437.gcn3>
- de Ugarte Postigo, A., Tanvir, N. R., Cano, Z., et al. 2016a, GCN Circ. 19245. <http://gcn.gsfc.nasa.gov/gcn/gcn3/19245.gcn3>
- de Ugarte Postigo, A., & Tomasella, L. 2015, GCN Circ. 17710. <http://gcn.gsfc.nasa.gov/gcn/gcn3/17710.gcn3>
- de Ugarte Postigo, A., Goldoni, P., Milvang-Jensen, B., et al. 2011, GCN Circ. 11579. <http://gcn.gsfc.nasa.gov/gcn/gcn3/11579.gcn3>
- de Ugarte Postigo, A., Thoene, C. C., Malesani, D., et al. 2014, GCN Circ. 16902. <http://gcn.gsfc.nasa.gov/gcn/gcn3/16902.gcn3>
- de Ugarte Postigo, A., Malesani, D., Perley, D. A., et al. 2016b, GCN Circ. 20150. <http://gcn.gsfc.nasa.gov/gcn/gcn3/20150.gcn3>
- de Ugarte Postigo, A., Izzo, L., Kann, D. A., et al. 2017c, GCN Circ. 20584. <http://gcn.gsfc.nasa.gov/gcn/gcn3/20584.gcn3>
- D'Elia, V., Covino, S., & D'Avanzo, P. 2008, GCN Circ. 8438. <http://gcn.gsfc.nasa.gov/gcn/gcn3/8438.gcn3>
- D'Elia, V., Xu, D., de Ugarte Postigo, A., et al. 2012, GCN Circ. 13507. <http://gcn.gsfc.nasa.gov/gcn/gcn3/13507.gcn3>
- Efron, B., & Petrosian, V. 1992, ApJ, 399, 345, doi: 10.1086/171931
- Fatkullin, T., Gorosabel, J., de Ugarte Postigo, A., et al. 2009, GCN Circ. 9712. <http://gcn.gsfc.nasa.gov/gcn/gcn3/9712.gcn3>
- Filgas, R., Tautenburg, T., Kupcu-Yoldas, A., et al. 2008, GCN Circ. 7747. <http://gcn.gsfc.nasa.gov/gcn/gcn3/7747.gcn3>
- Flores, H., Covino, S., de Ugarte Postigo, A., et al. 2013, GCN Circ. 14493. <http://gcn.gsfc.nasa.gov/gcn/gcn3/14493.gcn3>
- Flores, H., Fynbo, J. P. U., de Ugarte Postigo, A., et al. 2010, GCN Circ. 11317. <http://gcn.gsfc.nasa.gov/gcn/gcn3/11317.gcn3>

- Foley, S., Watson, D., Gorosabel, J., et al. 2006, A&A, 447, 891, doi: 10.1051/0004-6361:20054382
- Frail, D. A., Cameron, P. B., Kasliwal, M., et al. 2006, ApJ, 646, L99, doi: 10.1086/506934
- Frederiks, D. D., Hurley, K., Svinkin, D. S., et al. 2013, ApJ, 779, 151, doi: 10.1088/0004-637X/779/2/151
- Fynbo, J. P. U., Greiner, J., Kruehler, T., et al. 2008, GCN Circ. 8225, 1. <http://gcn.gsfc.nasa.gov/gcn/gcn3/8225.gcn3>
- Fynbo, J. P. U., Jakobsson, P., Prochaska, J. X., et al. 2009a, ApJS, 185, 526
- Fynbo, J. P. U., Malesani, D., Jakobsson, P., & D'Elia, V. 2009b, GCN Circ. 9947. <http://gcn.gsfc.nasa.gov/gcn/gcn3/9947.gcn3>
- Fynbo, J. P. U., Xu, D., Malesani, D., et al. 2013, GCN Circ. 14286. <http://gcn.gsfc.nasa.gov/gcn/gcn3/14286.gcn3>
- Gehrels, N., Chincarini, G., Giommi, P., et al. 2004, ApJ, 611, 1005, doi: 10.1086/422091
- Ghirlanda, G., Nava, L., Ghisellini, G., & Firmani, C. 2007, A&A, 466, 127, doi: 10.1051/0004-6361:20077119
- Goldoni, P., de Ugarte Postigo, A., & Fynbo, J. P. U. 2013, GCN Circ. 15571. <http://gcn.gsfc.nasa.gov/gcn/gcn3/15571.gcn3>
- Gorosabel, J., de Ugarte Postigo, A., Thoene, C. C., et al. 2014, GCN Circ. 17234. <http://gcn.gsfc.nasa.gov/gcn/gcn3/17234.gcn3>
- Grazian, A., Fernandez-Soto, A., Testa, V., et al. 2006, GCN Circ. 4545. <http://gcn.gsfc.nasa.gov/gcn/gcn3/4545.gcn3>
- Greiner, J., Clemens, C., Krühler, T., et al. 2009a, A&A, 498, 89
- Greiner, J., Krühler, T., McBreen, S., et al. 2009b, ApJ, 693, 1912, doi: 10.1088/0004-637X/693/2/1912
- Hanish, D. J., Meurer, G. R., Ferguson, H. C., et al. 2006, ApJ, 649, 150, doi: 10.1086/504681
- Hartoog, O. E., Malesani, D., Wiersema, K., et al. 2012, GCN Circ. 13730. <http://gcn.gsfc.nasa.gov/gcn/gcn3/13730.gcn3>
- Hjorth, J., Malesani, D., Jakobsson, P., et al. 2012, ApJ, 756, 187, doi: 10.1088/0004-637X/756/2/187
- Hopkins, A. M. 2004, ApJ, 615, 209, doi: 10.1086/424032

- Izzo, L., Cano, Z., de Ugarte Postigo, A., et al. 2017a, GCN Circ. 22039. <http://gcn.gsfc.nasa.gov/gcn/gcn3/22039.gcn3>
- Izzo, L., Selsing, J., Japelj, J., et al. 2017b, GCN Circ. 3368. <http://gcn.gsfc.nasa.gov/gcn/gcn3/3368.gcn3>
- Izzo, L., Heintz, K. E., Malesani, D., et al. 2018, GCN Circ. 22567, 1. <http://gcn.gsfc.nasa.gov/gcn/gcn3/22567.gcn3>
- Jakobsson, P., de Ugarte Postigo, A., Gorosabel, J., et al. 2009, GCN Circ. 9797. <http://gcn.gsfc.nasa.gov/gcn/gcn3/9797.gcn3>
- Jakobsson, P., Levan, A., Fynbo, J. P. U., et al. 2006, in American Institute of Physics Conference Series, Vol. 836, Gamma-Ray Bursts in the Swift Era, ed. S. S. Holt, N. Gehrels, & J. A. Nousek, 552–557, doi: 10.1063/1.2207953
- Jakobsson, P., Hjorth, J., Malesani, D., et al. 2012, ApJ, 752, 62, doi: 10.1088/0004-637X/752/1/62
- Jeong, S., Sanchez-Ramirez, R., Gorosabel, J., & Castro-Tirado, A. J. 2014, GCN Circ. 15936. <http://gcn.gsfc.nasa.gov/gcn/gcn3/15936.gcn3>
- Kann, D. A., Klose, S., Zhang, B., et al. 2010, ApJ, 720, 1513, doi: 10.1088/0004-637X/720/2/1513
- Kawai, N., Kosugi, G., Aoki, K., et al. 2006, Nature, 440, 184, doi: 10.1038/nature04498
- Knust, F., Kruehler, T., Klose, S., & Greiner, J. 2012, GCN Circ. 13810. <http://gcn.gsfc.nasa.gov/gcn/gcn3/13810.gcn3>
- Kozlova, A. V., Svinkin, D. S., Lysenko, A. L., et al. 2019, in Journal of Physics Conference Series, Vol. 1400, Journal of Physics Conference Series, 022014, doi: 10.1088/1742-6596/1400/2/022014
- Kruehler, T., Fynbo, J. P. U., Milvang-Jensen, B., Tanvir, N., & Jakobsson, P. 2012a, GCN Circ. 13134. <http://gcn.gsfc.nasa.gov/gcn/gcn3/13134.gcn3>
- Kruehler, T., Malesani, D., de Ugarte Postigo, A., Melandri, A., & Fynbo, J. P. U. 2014a, GCN Circ. 16194. <http://gcn.gsfc.nasa.gov/gcn/gcn3/16194.gcn3>
- Kruehler, T., Malesani, D., Xu, D., et al. 2013, GCN Circ. 14264. <http://gcn.gsfc.nasa.gov/gcn/gcn3/14264.gcn3>
- Kruehler, T., Vreeswijk, P. M., & Fynbo, J. P. U. 2014b, GCN Circ. 16401. <http://gcn.gsfc.nasa.gov/gcn/gcn3/16401.gcn3>

- Kruehler, T., Tanvir, N. R., de Ugarte Postigo, A., et al. 2012b, GCN Circ. 13930. <http://gcn.gsfc.nasa.gov/gcn/gcn3/13930.gcn3>
- Kröhler, T., Schady, P., Greiner, J., et al. 2011a, A&A, 526, A153, doi: [10.1051/0004-6361/201015327](https://doi.org/10.1051/0004-6361/201015327)
- Kröhler, T., Greiner, J., Schady, P., et al. 2011b, A&A, 534, A108, doi: [10.1051/0004-6361/201117428](https://doi.org/10.1051/0004-6361/201117428)
- Kröhler, T., Malesani, D., Milvang-Jensen, B., et al. 2012, ApJ, 758, 46, doi: [10.1088/0004-637X/758/1/46](https://doi.org/10.1088/0004-637X/758/1/46)
- Kröhler, T., Malesani, D., Fynbo, J. P. U., et al. 2015, A&A, 581, A125, doi: [10.1051/0004-6361/201425561](https://doi.org/10.1051/0004-6361/201425561)
- Laskar, T., Berger, E., Tanvir, N., et al. 2014, ApJ, 781, 1, doi: [10.1088/0004-637X/781/1/1](https://doi.org/10.1088/0004-637X/781/1/1)
- Levan, A. J., Jakobsson, P., Thoene, C. C., et al. 2009, GCN Circ. 9409. <http://gcn.gsfc.nasa.gov/gcn/gcn3/9409.gcn3>
- Levesque, E., Chornock, R., Kewley, L., et al. 2009, GCN Circ. 9264. <http://gcn.gsfc.nasa.gov/gcn/gcn3/9264.gcn3>
- Li, L.-X. 2008, MNRAS, 388, 1487, doi: [10.1111/j.1365-2966.2008.13488.x](https://doi.org/10.1111/j.1365-2966.2008.13488.x)
- Lien, A., Sakamoto, T., Barthelmy, S. D., et al. 2016, ApJ, 829, 7, doi: [10.3847/0004-637X/829/1/7](https://doi.org/10.3847/0004-637X/829/1/7)
- Lloyd-Ronning, N. M., Aykutalp, A., & Johnson, J. L. 2019, MNRAS, 488, 5823, doi: [10.1093/mnras/stz2155](https://doi.org/10.1093/mnras/stz2155)
- Lloyd-Ronning, N. M., Fryer, C. L., & Ramirez-Ruiz, E. 2002, ApJ, 574, 554, doi: [10.1086/341059](https://doi.org/10.1086/341059)
- Lynden-Bell, D. 1971, MNRAS, 155, 95, doi: [10.1093/mnras/155.1.95](https://doi.org/10.1093/mnras/155.1.95)
- Malesani, D., Fynbo, J. P. U., Heintz, K. E., Stone, M., & Karhunen, K. 2017, GCN Circ. 22039. <http://gcn.gsfc.nasa.gov/gcn/gcn3/22039.gcn3>
- Malesani, D., Kruehler, T., Perley, D., et al. 2013, GCN Circ. 14225. <http://gcn.gsfc.nasa.gov/gcn/gcn3/14225.gcn3>
- Malesani, D., Schulze, S., de Ugarte Postigo, A., et al. 2012, GCN Circ. 13649. <http://gcn.gsfc.nasa.gov/gcn/gcn3/13649.gcn3>
- Markwardt, C. B. 2009, in Astronomical Society of the Pacific Conference Series, Vol. 411, Astronomical Data Analysis Software and Systems XVIII, ed. D. A. Bohlender, D. Durand, & P. Dowler, 251. <https://arxiv.org/abs/0902.2850>

- Markwardt, C. B., Barthelmy, S. D., Cummings, J. C., et al. 2007, The SWIFT BAT Software Guide. http://swift.gsfc.nasa.gov/analysis/bat_swguide_v6_3.pdf
- Marshall, F. E., & Page, K. L. 2014, GCN Circ. 16241. <http://gcn.gsfc.nasa.gov/gcn/gcn3/16241.gcn3>
- Mirabal, N., Halpern, J. P., & O'Brien, P. T. 2007, ApJ, 661, L127, doi: 10.1086/519006
- Moskvitin, A., Burenin, R., Uklein, R., et al. 2014, GCN Circ. 16489. <http://gcn.gsfc.nasa.gov/gcn/gcn3/16489.gcn3>
- Oates, S. R., Page, M. J., Schady, P., et al. 2009, MNRAS, 395, 490, doi: 10.1111/j.1365-2966.2009.14544.x
- Penprase, B. E., Berger, E., Fox, D. B., et al. 2006, ApJ, 646, 358, doi: 10.1086/504678
- Perley, D. A., Bloom, J. S., & Prochaska, J. X. 2013a, in EAS Publications Series, Vol. 61, EAS Publications Series, ed. A. J. Castro-Tirado, J. Gorosabel, & I. H. Park, 391–395, doi: 10.1051/eas/1361062
- Perley, D. A., Malesani, D. B., Fynbo, J. P. U., et al. 2018, GCN Circ. 23421, 1. <http://gcn.gsfc.nasa.gov/gcn/gcn3/23421.gcn3>
- Perley, D. A., Prochaska, J. X., & Morgan, A. N. 2012, GCN Circ. 14059. <http://gcn.gsfc.nasa.gov/gcn/gcn3/14059.gcn3>
- Perley, D. A., Levan, A. J., Tanvir, N. R., et al. 2013b, ApJ, 778, 128, doi: 10.1088/0004-637X/778/2/128
- Pescalli, A., Ghirlanda, G., Salvaterra, R., et al. 2016, A&A, 587, A40, doi: 10.1051/0004-6361/201526760
- Petrosian, V., Kitanidis, E., & Kocevski, D. 2015, ApJ, 806, 44, doi: 10.1088/0004-637X/806/1/44
- Planck Collaboration, Ade, P. A. R., Aghanim, N., et al. 2014, A&A, 571, A16, doi: 10.1051/0004-6361/201321591
- Press, W. H., Teukolsky, S. A., Vetterling, W. T., & Flannery, B. P. 1992, Numerical recipes in C. The art of scientific computing (Cambridge University Press)
- Prochaska, J. X., Bloom, J. S., Chen, H.-W., et al. 2005, GCN Circ. 3700. <http://gcn.gsfc.nasa.gov/gcn/gcn3/3700.gcn3>
- Prochaska, J. X., Chen, H.-W., Bloom, J. S., Falco, E., & Dupree, A. K. 2006, GCN Circ. 5002. <http://gcn.gsfc.nasa.gov/gcn/gcn3/5002.gcn3>
- Rau, A., Fynbo, J., & Greiner, J. 2010, GCN Circ. 10350. <http://gcn.gsfc.nasa.gov/gcn/gcn3/10350.gcn3>

- Roming, P. W. A., Kennedy, T. E., Mason, K. O., et al. 2005, Space Sci. Rev., 120, 95, doi: 10.1007/s11214-005-5095-4
- Rossi, A., Gargiulo, A., Malesani, D. B., et al. 2018, GRB Coordinates Network, 22845, 1
- Rossi, A., Piranomonte, S., Savaglio, S., et al. 2014, A&A, 572, A47, doi: 10.1051/0004-6361/201423865
- Sakamoto, T., Barthelmy, S. D., Barbier, L., et al. 2008, ApJS, 175, 179, doi: 10.1086/523646
- Sakamoto, T., Sato, G., Barbier, L., et al. 2009, ApJ, 693, 922, doi: 10.1088/0004-637X/693/1/922
- Sakamoto, T., Barthelmy, S. D., Baumgartner, W. H., et al. 2011a, ApJS, 195, 2, doi: 10.1088/0067-0049/195/1/2
- Sakamoto, T., Pal'Shin, V., Yamaoka, K., et al. 2011b, PASJ, 63, 215, doi: 10.1093/pasj/63.1.215
- Salvaterra, R., Della Valle, M., Campana, S., et al. 2009, Nature, 461, 1258, doi: 10.1038/nature08445
- Sanchez-Ramirez, R., Gorosabel, J., de Ugarte Postigo, A., & Gonzalez Perez, J. M. 2012a, GCN Circ. 13723. <http://gcn.gsfc.nasa.gov/gcn/gcn3/13723.gcn3>
- Sanchez-Ramirez, R., Oates, S. R., Tello, J. C., et al. 2016, GCN Circ. 18925. <http://gcn.gsfc.nasa.gov/gcn/gcn3/18925.gcn3>
- Sanchez-Ramirez, R., de Ugarte Postigo, A., Kruehler, T., et al. 2012b, GCN Circ. 14035. <http://gcn.gsfc.nasa.gov/gcn/gcn3/14035.gcn3>
- Sánchez-Ramírez, R., Gorosabel, J., de Ugarte Postigo, A., et al. 2013, in Revista Mexicana de Astronomía y Astrofísica, vol. 27, Vol. 42, Revista Mexicana de Astronomía y Astrofísica Conference Series, 113–113
- Sanchez-Ramirez, R., Gorosabel, J., Perez-Ramirez, D., et al. 2015, GCN Circ. 18177. <http://gcn.gsfc.nasa.gov/gcn/gcn3/18177.gcn3>
- Scargle, J. D., Norris, J. P., Jackson, B., & Chiang, J. 2013, ApJ, 764, 167, doi: 10.1088/0004-637X/764/2/167
- Schmidl, S., Kann, D. A., & Greiner, J. 2013, GCN Circ. 14634. <http://gcn.gsfc.nasa.gov/gcn/gcn3/14634.gcn3>
- Selsing, J., Malesani, D., Kann, D. A., & Tanvir, N. R. 2018, GCN Circ. 22591, 1. <http://gcn.gsfc.nasa.gov/gcn/gcn3/22591.gcn3>
- Smette, A., Ledoux, C., Vreeswijk, P., et al. 2013, GCN Circ. 14848. <http://gcn.gsfc.nasa.gov/gcn/gcn3/14848.gcn3>

- Sparre, M., de Ugarte Postigo, A., Fynbo, J. P. U., et al. 2011, GCN Circ. 11607. <http://gcn.gsfc.nasa.gov/gcn/gcn3/11607.gcn3>
- Svinkin, D. S., Frederiks, D. D., Aptekar, R. L., et al. 2016, ApJS, 224, 10, doi: 10.3847/0067-0049/224/1/10
- Tanvir, N. R., Fox, D., Fynbo, J., & Trujillo, C. 2012a, GCN Circ. 13562. <http://gcn.gsfc.nasa.gov/gcn/gcn3/13562.gcn3>
- Tanvir, N. R., Fynbo, J. P. U., Melandri, A., et al. 2012b, GCN Circ. 13890. <http://gcn.gsfc.nasa.gov/gcn/gcn3/13890.gcn3>
- Tanvir, N. R., Kruehler, T., Wiersema, K., et al. 2016, GCN Circ. 20321. <http://gcn.gsfc.nasa.gov/gcn/gcn3/20321.gcn3>
- Tanvir, N. R., Levan, A. J., & Coulson, D. 2014a, GCN Circ. 16570. <http://gcn.gsfc.nasa.gov/gcn/gcn3/16570.gcn3>
- Tanvir, N. R., Levan, A. J., Wiersema, K., et al. 2014b, GCN Circ. 16150. <http://gcn.gsfc.nasa.gov/gcn/gcn3/16150.gcn3>
- Tanvir, N. R., Wiersema, K., Xu, D., & Fynbo, J. P. U. 2013, GCN Circ. 14882. <http://gcn.gsfc.nasa.gov/gcn/gcn3/14882.gcn3>
- Tanvir, N. R., Heintz, K. E., Selsing, J., et al. 2018, GCN Circ. 22384, 1. <http://gcn.gsfc.nasa.gov/gcn/gcn3/22384.gcn3>
- Tello, J. C., Sanchez-Ramirez, R., Gorosabel, J., et al. 2012, GCN Circ. 13118. <http://gcn.gsfc.nasa.gov/gcn/gcn3/13118.gcn3>
- Thoene, C. C., & de Ugarte Postigo, A. 2014, GCN Circ. 16079. <http://gcn.gsfc.nasa.gov/gcn/gcn3/16079.gcn3>
- Thoene, C. C., de Ugarte Postigo, A., Gorosabel, J., et al. 2012, GCN Circ. 13628. <http://gcn.gsfc.nasa.gov/gcn/gcn3/13628.gcn3>
- Thoene, C. C., Perley, D. A., Cooke, J., et al. 2007, GCN Circ. 6741. <http://gcn.gsfc.nasa.gov/gcn/gcn3/6741.gcn3>
- Thompson, R. I., Eisenstein, D., Fan, X., et al. 2006, ApJ, 647, 787, doi: 10.1086/505568
- Tsvetkova, A., Frederiks, D., Golenetskii, S., et al. 2017, ApJ, 850, 161, doi: 10.3847/1538-4357/aa96af
- Vergani, S. D., D'Avanzo, P., Malesani, D., et al. 2010, GCN Circ. 10495. <http://gcn.gsfc.nasa.gov/gcn/gcn3/10495.gcn3>

- Wang, X.-G., Zhang, B., Liang, E.-W., et al. 2018, ApJ, 859, 160, doi: 10.3847/1538-4357/aabc13
- Williams, M. J., Bureau, M., & Cappellari, M. 2010, MNRAS, 409, 1330, doi: 10.1111/j.1365-2966.2010.17406.x
- Wu, S.-W., Xu, D., Zhang, F.-W., & Wei, D.-M. 2012, MNRAS, 423, 2627, doi: 10.1111/j.1365-2966.2012.21068.x
- Xu, D., Fynbo, J. P. U., D’Elia, V., & Tanvir, N. R. 2012, GCN Circ. 13460. <http://gcn.gsfc.nasa.gov/gcn/gcn3/13460.gcn3>
- Xu, D., Fynbo, J. P. U., Malesani, D., et al. 2016, GCN Circ. 19109. <http://gcn.gsfc.nasa.gov/gcn/gcn3/19109.gcn3>
- Xu, D., Heintz, K. E., Malesani, D., & Fynbo, J. P. U. 2017, GCN Circ. 20458. <http://gcn.gsfc.nasa.gov/gcn/gcn3/20458.gcn3>
- Xu, D., Tanvir, N. R., Malesani, D., et al. 2015, GCN Circ. 18696. <http://gcn.gsfc.nasa.gov/gcn/gcn3/18696.gcn3>
- Xu, D., Vreeswijk, P. M., Fynbo, J. P. U., et al. 2014, GCN Circ. 17040. <http://gcn.gsfc.nasa.gov/gcn/gcn3/17040.gcn3>
- Xu, D., Malesani, D., Kruehler, T., et al. 2013a, GCN Circ. 14273. <http://gcn.gsfc.nasa.gov/gcn/gcn3/14273.gcn3>
- Xu, D., Malesani, D., Schulze, S., et al. 2013b, GCN Circ. 15451. <http://gcn.gsfc.nasa.gov/gcn/gcn3/15451.gcn3>
- Yonetoku, D., Murakami, T., Nakamura, T., et al. 2004, ApJ, 609, 935, doi: 10.1086/421285
- Yu, H., Wang, F. Y., Dai, Z. G., & Cheng, K. S. 2015, ApJS, 218, 13, doi: 10.1088/0067-0049/218/1/13
- Zheng, W., Filippenko, A. V., Yuk, H., Zhu, Y., & Perley, D. A. 2015, GCN Circ. 18273, 1. <http://gcn.gsfc.nasa.gov/gcn/gcn3/18273.gcn3>

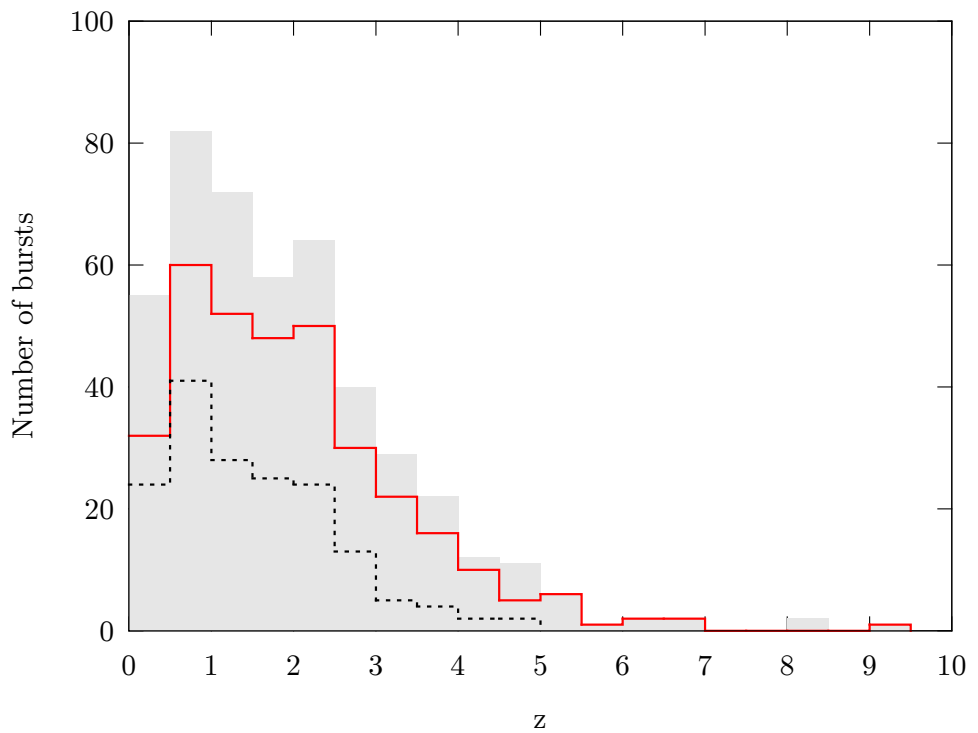


Fig. 1.— GRB redshift distributions up to Jan 2019. Gray shaded area: all 469 GRBs with known redshifts (“GRBOX”). The red line: 338 KW GRBs (both triggered and waiting mode). The black dotted line: 171 KW triggered bursts.

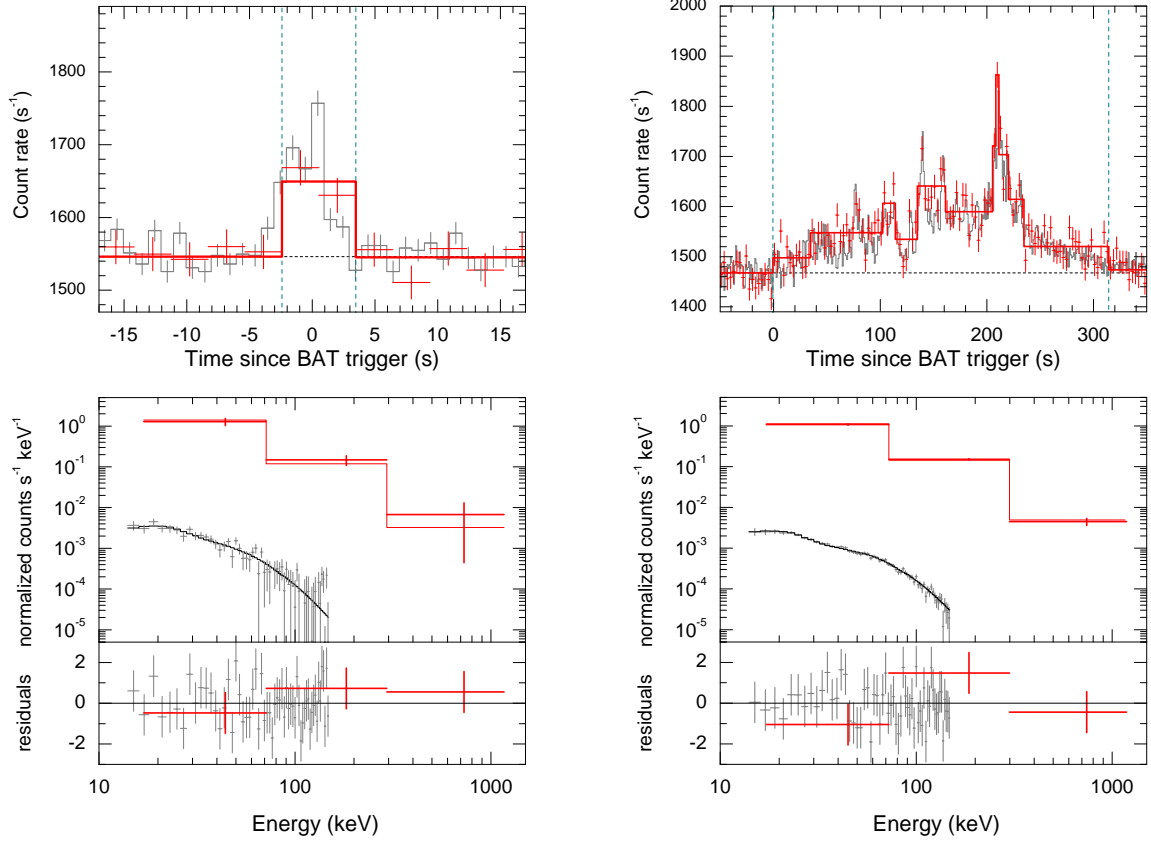


Fig. 2.— Joint KW and BAT detections of GRB 090429B at $z=9.38$ (left) and GRB 110205A at $z=2.22$ (right). The burst light curves are presented in the top panels. The KW waiting-mode count rates ($G1+G2$, $\sim 20\text{--}350$ keV) are shown with red points, and the horizontal dashed lines indicate KW background levels. The BAT count rates (25–350 keV), arbitrary scaled to match the KW count rate and background, are shown with gray points and lines. Bayesian block divisions of the KW light curves are plotted with thick red lines. The vertical dashed lines indicate time intervals chosen for time-integrated spectral fits. Joint KW+BAT fits to the TI spectra and the fit residuals are presented lower panels, where KW and BAT spectral points are shown by red and gray points, respectively. The best-fit models (Table 2) are plotted by solid lines: the Band function, with $\alpha \simeq -0.7$, $\beta \simeq -2.3$ and $E_p \simeq 41$ keV, for GRB 090429B; and CPL ($\alpha \simeq -1.55$, $E_p \simeq 220$ keV) for GRB 110205A.

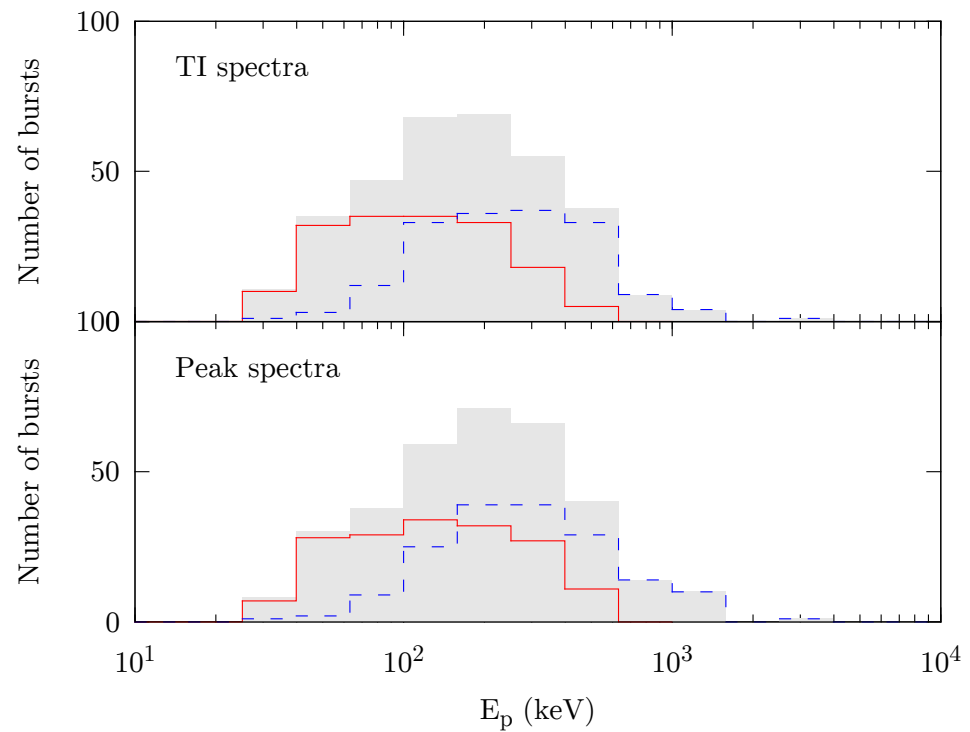


Fig. 3.— Distributions of E_p (observer frame) for the WM sample (red solid lines), the KW triggered sample (blue dashed lines), and the whole KW sample of GRBs with known redshifts (the gray shaded areas).

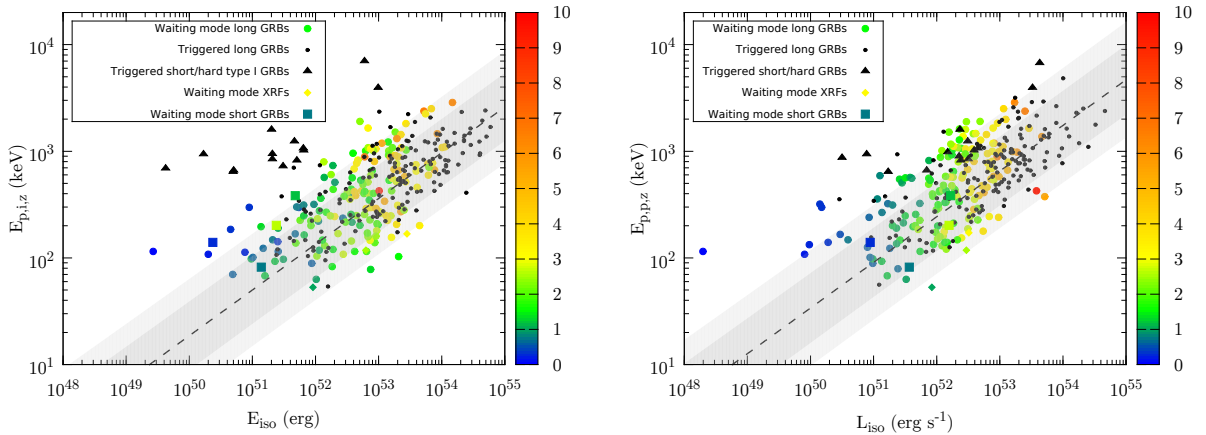


Fig. 4.— Rest-frame energetics of 338 KW GRBs in the $E_{\text{iso}} - E_{\text{p},\text{i},\text{z}}$ (left) and $L_{\text{iso}} - E_{\text{p},\text{p},\text{z}}$ (right) planes. Black symbols: KW triggered bursts. Colored symbols: the WM sample (this work); the color of each data point represents the GRB redshift. The “Amati” and “Yonetoku” relations calculated for 315 KW long (type II) GRBs are plotted with dashed lines, and the dark- and light-gray shaded areas show their 68% and 90% PI’s, respectively.

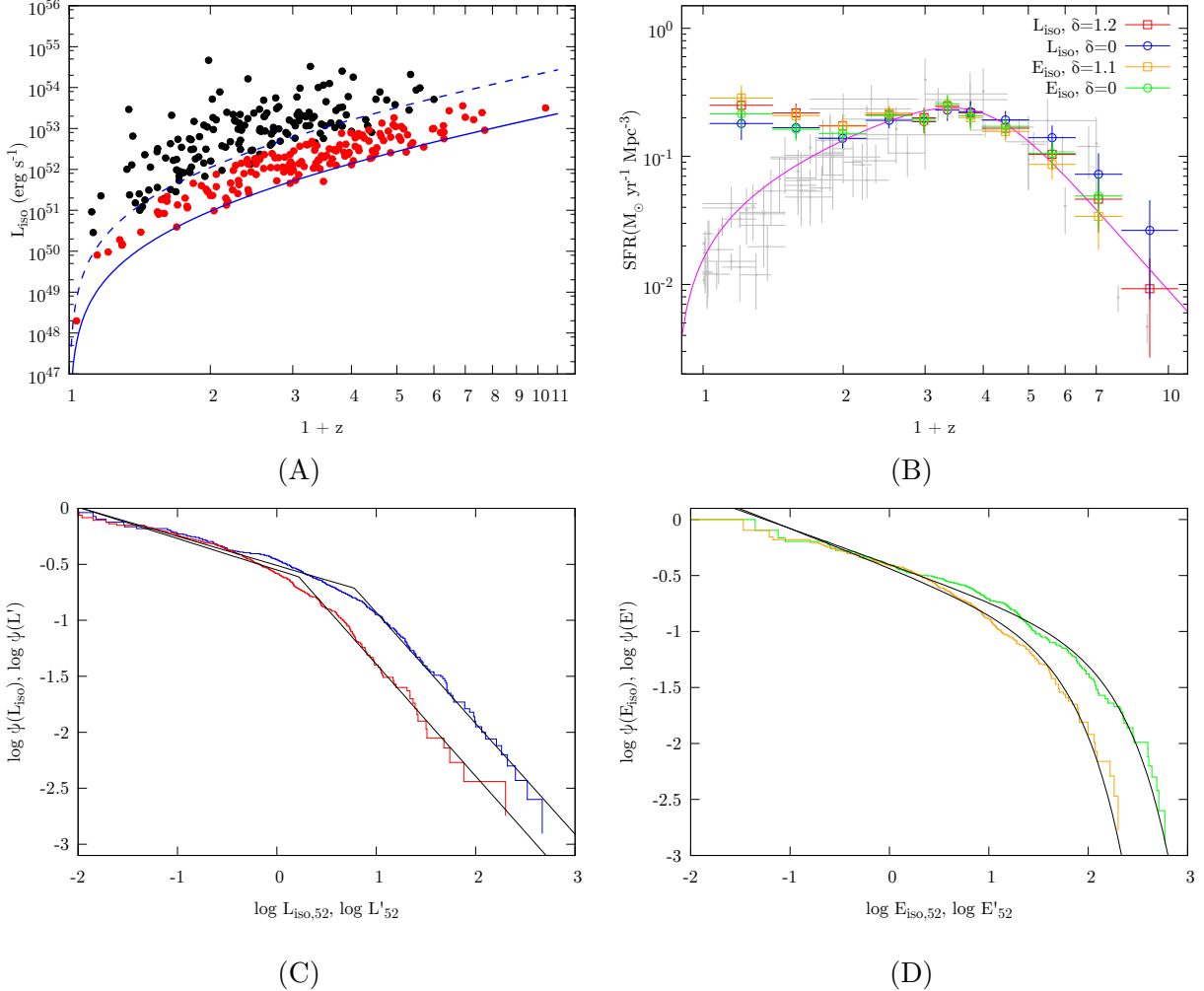


Fig. 5.— Panel A: L_{iso} vs. redshift for 315 KW GRBs. Black symbols: 171 triggered bursts (the updated T17 sample). Red symbols: the WM sample (167 bursts, this work). The observer-frame flux limits F_{peak} (Section 5.3) are shown by a dashed line (triggered bursts) and a solid line (the full KW sample). Panel B: Comparison of the derived GRBFR and the SFR data from the literature. The gray points show the SFR data from Hopkins (2004), Bouwens et al. (2011), Hanish et al. (2006), and Thompson et al. (2006). The solid line denotes the SFR approximation from Li (2008). The GRBFR normalization is the same for the results derived using the four datasets and the GRBFR points have been shifted arbitrarily to match the SFR at $(1+z) \sim 3.5$. Panel C shows cumulative GRB isotropic-luminosity functions (LFs: $\psi(L_{\text{iso}})$ - blue, $\psi(L')$ - red) and their BPL approximations (black). Panel D shows cumulative GRB isotropic-energy functions (EFs: $\psi(E_{\text{iso}})$ - green, $\psi(E')$ - orange) and their exponentially cutoff PL approximations (black). The distributions (Section 5.3) are normalized to unity at the dimmest points. The approximation parameters are given in Table 7.

Table 1. Joint KW/*Swift*-BAT sample

Burst name	<i>Swift</i> trigger #	Trigger time ^a	<i>z</i>	<i>z</i> type ^b	<i>z</i> ref	<i>t</i> ₀ (s)	<i>T</i> ₁₀₀ (s)
GRB 050126	103780	12:00:54.073	1.290	s	(1)	-0.240	40.000
GRB 050219A	106415	12:40:01.049	0.211	s	(2)	-5.816	27.072
GRB 050315	111063	20:59:42.519	1.9500	s	(3)	-56.240	105.408
GRB 050318	111529	15:44:37.171	1.4436	s	(3)	-0.600	32.992
GRB 050505	117504	23:22:21.099	4.27	s	(4)	-10.648	62.656
GRB 050724	147478	12:34:09.362	0.258	s	(5)	-0.056	2.096
GRB 050730	148225	19:58:23.199	3.9693	s	(6)	-61.064	181.504
GRB 050802	148646	10:08:02.267	1.7102	s	(6)	-3.408	22.976
GRB 050803	148833	19:14:00.344	0.422	s	(7)	59.592	138.944
GRB 050814	150314	11:38:56.966	5.3	p	(8)	-1.272	108.544
GRB 050826	152113	06:18:10.289	0.296	s	(9)	-0.208	39.224
GRB 050904	153514	01:51:44.290	6.295	s	(10)	19.688	195.456
GRB 051006	158593	20:30:33.256	1.059	s	(11)	-3.472	35.264
GRB 051111	163438	05:59:41.479	1.54948	s	(12)	-5.872	87.040
GRB 060111A	176818	04:23:06.123	2.32	s	(13)	-0.640	13.440
GRB 060115	177408	13:08:00.643	3.5328	s	(6)	-50.192	158.336
GRB 060116	177533	08:37:27.233	6.60	p	(14)	-55.160	94.208
GRB 060202	179968	08:40:55.008	0.785	s	(15)	-32.632	224.512
GRB 060206	180455	04:46:53.273	4.0559	s	(6)	-0.584	7.040
GRB 060210	180977	04:58:49.809	3.9122	s	(6)	-229.416	353.792
GRB 060223A	192059	06:04:23.928	4.406	s	(16)	-2.040	12.096
GRB 060306	200638	00:49:10.626	1.551	s	(15)	-1.312	68.416
GRB 060418	205851	03:06:08.204	1.4901	s	(17)	-19.440	160.192
GRB 060526	211957	16:28:29.951	3.2213	s	(6)	-1.344	10.176
GRB 060602A	213180	21:32:12.464	0.787	s	(18)	1.072	73.792
GRB 060607A	213823	05:12:13.352	3.0749	s	(6)	-16.104	122.368
GRB 060707	217704	21:30:19.497	3.4240	s	(6)	-51.832	106.240
GRB 060708	217805	12:15:59.016	1.92	p	(19)	-1.304	7.936
GRB 060714	219101	15:12:00.283	2.7108	s	(6)	-11.696	132.416
GRB 060729	221755	19:12:29.244	0.5428	s	(6)	-0.808	125.760
GRB 060801	222154	12:16:15.159	1.1304 ^c	s	(20)	-0.512	1.960
GRB 060904B	228006	02:31:03.858	0.7029	s	(6)	-0.944	28.664
GRB 060906	228316	08:32:46.573	3.6856	s	(6)	-40.000	49.448
GRB 060908	228581	08:57:22.345	1.8836	s	(6)	-10.208	22.656
GRB 060923A	230662	05:12:15.370	2.6	p	(15)	-42.264	56.384
GRB 060927	231362	14:07:35.297	5.4636	s	(6)	-1.112	25.408
GRB 061110B	238174	21:58:45.541	3.4344	s	(6)	-16.256	147.578
GRB 070110	255445	07:22:41.574	2.3521	s	(6)	-2.784	93.632
GRB 070208	259714	09:10:34.281	1.165	s	(21)	-4.032	55.176
GRB 070318	271019	07:28:56.089	0.8397	s	(6)	-0.880	59.809
GRB 070411	275087	20:12:33.316	2.9538	s	(6)	-16.416	107.904
GRB 070419B	276212	10:44:05.972	1.9588	s	(22)	-12.608	275.136
GRB 070529	280706	12:48:28.349	2.4996	s	(23)	0.664	120.192
GRB 070611	282003	01:57:13.890	2.0394	s	(6)	-3.232	10.560
GRB 070612A	282066	02:38:45.984	0.617	s	(24)	-5.976	281.664

Table 1—Continued

Burst name	<i>Swift</i> trigger #	Trigger time ^a	<i>z</i>	<i>z</i> type ^b	<i>z</i> ref	<i>t</i> ₀ (s)	<i>T</i> ₁₀₀ (s)
GRB 070721B	285654	10:33:46.314	3.6298	s	(6)	-6.712	371.136
GRB 070810A	287364	02:11:52.415	2.17	s	(25)	-2.120	6.400
GRB 071021	294974	09:41:33.694	2.4520	s	(22)	-4.504	264.768
GRB 071025	295301	04:08:53.685	5.2 ^d	s+p	(6)	40.104	152.704
GRB 080129	301981	06:06:45.464	4.349	s	(26)	-1.704	38.976
GRB 080207	302728	21:30:21.442	2.0858	s	(22)	-1.112	343.112
GRB 080210	302888	07:50:05.436	2.6419	s	(6)	-14.560	62.400
GRB 080310	305288	08:37:58.647	2.4274	s	(6)	-9.712	21.765
GRB 080325	307604	04:09:17.332	1.78	s	(15)	-33.464	213.504
GRB 080430	310613	19:53:02.076	0.767	s	(27)	-0.408	20.352
GRB 080515	311658	06:01:13.817	2.47	s	(13)	-6.400	24.792
GRB 080516	311762	00:17:07.031	3.2	p	(28)	0.048	7.040
GRB 080604	313116	07:27:01.160	1.4171	s	(6)	-28.632	88.768
GRB 080707	316204	08:27:53.686	1.2322	s	(6)	-2.440	31.360
GRB 080804	319016	23:20:14.670	2.2045	s	(6)	-0.496	38.784
GRB 080805	319036	07:41:34.733	1.5042	s	(6)	-3.888	96.832
GRB 080810	319584	13:10:12.288	3.3604	s	(6)	-14.016	120.256
GRB 080905B	323898	16:55:45.405	2.3739	s	(6)	-7.480	111.872
GRB 080906	323984	13:33:16.347	2.13	p	(29)	-117.888	235.008
GRB 080913	324561	06:46:54.122	6.7	s	(30)	-3.592	8.832
GRB 080928	326115	15:01:32.867	1.6919	s	(6)	56.808	268.352
GRB 081008	331093	19:58:09.385	1.9685	s	(31)	-65.160	207.104
GRB 081028A	332851	00:25:00.791	3.038	s	(32)	44.656	300.608
GRB 081029	332931	01:43:56.788	3.8479	s	(33)	-38.864	326.528
GRB 081109A	334112	07:02:06.615	0.9787	s	(34)	-18.096	95.488
GRB 090113	339852	18:40:39.171	1.7493	s	(22)	-0.160	10.112
GRB 090418A	349510	11:07:40.227	1.608	s	(35)	-8.216	69.184
GRB 090426	350479	12:48:47.213	2.609	s	(36)	-0.032	0.832
GRB 090429B	350854	05:30:03.366	9.38	p	(37)	-3.064	6.000
GRB 090516A	352190	08:27:50.774	4.109	s	(38)	-8.544	234.560
GRB 090519	352648	21:08:56.429	3.85	s	(39)	-12.432	86.976
GRB 090530	353567	03:18:18.384	1.266	s	(40)	-0.224	41.600
GRB 090726	358422	22:42:27.759	2.71	s	(41)	-22.879	61.824
GRB 090814A	359951	00:52:19.004	0.696 ^e	s	(42)	-15.200	61.248
GRB 090926B	370791	21:55:48.416	1.24	s	(43)	-21.352	154.496
GRB 091018	373172	20:48:19.585	0.971	s	(44)	-0.376	5.184
GRB 091029	374210	03:53:22.596	2.752	s	(45)	-10.176	50.432
GRB 091109A	375246	04:57:43.364	3.076	s	(46)	-0.824	24.832
GRB 100316A	416076	02:23:00.430	3.155	s	(47)	-1.032	7.040
GRB 100316B	416103	08:01:36.973	1.180	s	(48)	-0.360	4.672
GRB 100615A	424733	01:59:03.995	1.398	s	(49)	-0.080	47.488
GRB 100728B	430172	10:31:55.829	2.106	s	(50)	-1.712	14.912
GRB 100901A	433065	13:34:10.376	1.408	s	(51)	-2.776	444.800
GRB 101219B	440635	16:27:53.520	0.5519	s	(52)	15.720	26.496
GRB 110106B	441676	21:26:17.014	0.618	s	(53)	-3.008	24.448

Table 1—Continued

Burst name	<i>Swift</i> trigger #	Trigger time ^a	<i>z</i>	<i>z</i> type ^b	<i>z</i> ref	<i>t</i> ₀ (s)	<i>T</i> ₁₀₀ (s)
GRB 110128A	443861	01:44:33.009	2.339	s	(54)	-2.560	24.320
GRB 110205A	444643	02:02:41.367	2.22	s	(55)	21.416	356.544
GRB 110726A	458059	01:30:40.550	1.036 ^f	s	(56)	-0.064	3.776
GRB 110801A	458521	19:49:42.991	1.858	s	(57)	-24.232	412.160
GRB 110818A	500914	20:37:49.206	3.36	s	(58)	-13.048	77.440
GRB 111107A	507185	00:50:24.005	2.893	s	(59)	-0.064	37.440
GRB 111123A	508319	18:13:21.100	3.1516	s	(60)	-8.216	286.336
GRB 111225A	510341	03:50:37.792	0.297	s	(61)	-8.720	82.496
GRB 120118B	512003	17:00:21.195	2.943	s	(62)	-0.824	26.496
GRB 120326A	518626	01:20:29.280	1.798	s	(63)	-70.992	88.576
GRB 120327A	518731	02:55:16.636	2.813	s	(64)	-15.992	83.136
GRB 120404A	519380	12:51:02.399	2.876	s	(65)	-5.096	42.624
GRB 120521C	522656	23:22:07.703	6	p	(66)	-1.472	38.400
GRB 120712A	526351	13:42:27.382	4.1745	s	(67)	-4.600	22.272
GRB 120722A	528195	12:53:26.546	0.9586	s	(68)	-2.968	38.208
GRB 120802A	529486	08:00:51.628	3.796	s	(69)	-1.040	17.984
GRB 120811C	530689	15:34:52.170	2.671	s	(70)	-9.656	34.688
GRB 120815A	531003	02:13:58.782	2.358	s	(71)	-0.216	7.872
GRB 120907A	532871	00:24:23.082	0.970	s	(72)	-0.024	7.104
GRB 120909A	533060	01:42:03.235	3.93	s	(73)	-40.512	125.760
GRB 120922A	534394	22:30:28.657	3.1	p	(74)	-22.568	171.776
GRB 121024A	536580	02:56:12.478	2.298	s	(75)	-8.296	12.096
GRB 121027A	536831	07:32:29.747	1.773	s	(76)	-9.344	72.640
GRB 121201A	540178	12:25:42.065	3.385	s	(77)	-24.088	7.008
GRB 121211A	541200	13:47:02.795	1.023	s	(78)	-2.776	199.936
GRB 130131B	547420	19:10:08.907	2.539	s	(79)	-0.288	4.736
GRB 130420A	553977	07:28:29.538	1.297	s	(80)	-24.728	207.360
GRB 130427B	554635	13:20:41.799	2.78 ^g	s	(81)	-0.632	30.144
GRB 130511A	555600	11:30:47.442	1.3033	s	(82)	-0.048	3.328
GRB 130514A	555821	07:13:41.063	3.6	p	(83)	-7.680	281.344
GRB 130604A	557354	06:54:26.998	1.06	s	(84)	-0.624	34.816
GRB 130606A	557589	21:04:39.020	5.91	s	(85)	-1.104	165.970
GRB 130610A	557845	03:12:13.344	2.092	s	(86)	-6.688	67.688
GRB 130612A	557976	03:22:22.168	2.006	s	(87)	-0.504	3.264
GRB 131004A	573190	21:41:03.688	0.717	s	(88)	-0.248	1.344
GRB 131103A	576562	22:07:25.794	0.5955	s	(89)	-8.784	15.760
GRB 131227A	582184	04:44:51.212	5.3	s	(90)	-1.064	20.288
GRB 140114A	583861	11:57:40.482	3.0	s	(91)	24.296	141.056
GRB 140304A	590206	13:22:31.098	5.283	s	(92)	-3.912	19.456
GRB 140311A	591390	21:05:16.252	4.954	s	(93)	-4.440	85.184
GRB 140423A	596901	08:31:53.262	3.26	s	(94)	-67.472	182.080
GRB 140430A	597722	20:33:36.527	1.60	s	(95)	-0.344	29.864
GRB 140509A	598497	02:22:13.613	2.4	p	(96)	-3.312	29.312
GRB 140518A	599287	09:17:46.631	4.707	s	(97)	-4.632	64.704
GRB 140614A	601646	01:04:59.864	4.233	s	(98)	-96.600	184.768

Table 1—Continued

Burst name	<i>Swift</i> trigger #	Trigger time ^a	<i>z</i>	<i>z</i> type ^b	<i>z</i> ref	<i>t</i> ₀ (s)	<i>T</i> ₁₀₀ (s)
GRB 140629A	602884	14:17:30.327	2.275	s	(99)	-6.184	26.304
GRB 140703A	603243	00:37:17.064	3.14	s	(100)	-14.128	86.208
GRB 140710A	603954	10:16:40.041	0.558	s	(101)	-0.176	1.728
GRB 140907A	611933	16:07:08.847	1.21	s	(102)	-16.176	55.552
GRB 141004A	614390	23:20:54.395	0.573	s	(103)	-0.864	6.208
GRB 141109A	618024	05:49:55.236	2.993	s	(104)	-0.664	179.584
GRB 141225A	622476	23:01:07.035	0.915	s	(105)	4.904	28.352
GRB 150301B	633180	19:38:04.028	1.5169	s	(106)	-0.328	24.384
GRB 150413A	637899	13:54:58.559	3.139	s	(107)	-90.648	300.352
GRB 150818A	652603	11:36:32.926	0.282	s	(108)	-26.112	184.256
GRB 150910A	655097	09:04:48.886	1.359	s	(109)	32.616	90.752
GRB 151111A	663074	08:33:23.417	3.5	p	(110)	-5.128	90.752
GRB 151112A	663179	13:44:48.084	4.1	p	(111)	-0.064	14.784
GRB 151215A	667392	03:01:28.957	2.59	s	(112)	-0.216	3.264
GRB 160121A	671231	13:50:37.711	1.960	s	(113)	-0.016	12.864
GRB 160227A	676423	19:32:08.096	2.38	s	(114)	-20.056	287.168
GRB 160327A	680655	09:16:07.705	4.99	s	(115)	-6.400	42.176
GRB 161017A	718023	17:51:51.170	2.013	s	(116)	-4.632	240.832
GRB 161108A	721234	03:32:33.177	1.159	s	(117)	-4.296	130.048
GRB 161219B	727541	18:48:39.308	0.1475	s	(118)	-0.536	7.040
GRB 170113A	732526	10:04:05.482	1.968	s	(119)	-0.608	23.672
GRB 170202A	736407	18:28:02.373	3.645	s	(120)	0.328	50.744
GRB 170531B	755354	22:02:09.206	2.366	s	(121)	-0.056	171.904
GRB 170604A	755587	19:08:50.402	1.329	s	(122)	-11.672	30.592
GRB 171020A	780845	23:07:10.752	1.87	s	(123)	-0.968	28.352
GRB 171205A	794972	07:20:43.893	0.0368	s	(124)	-44.120	216.896
GRB 171222A	799669	16:24:59.804	2.409	s	(125)	4.968	205.120
GRB 180115A	805318	04:16:03.681	2.487	s	(126)	16.680	56.128
GRB 180205A	808625	04:25:29.332	1.409	s	(127)	-6.992	13.120
GRB 180329B	819490	14:08:23.971	1.998	s	(128)	-8.888	266.496
GRB 180404A	821881	00:45:35.687	1.000	s	(129)	-22.712	38.400
GRB 180624A	844192	13:49:40.379	2.855	s	(130)	-61.128	262.080
GRB 181110A	871316	08:43:31.320	1.505	s	(131)	-104.432	217.536

^a *Swift*/BAT trigger time.^b Redshift types are: s = spectroscopic, p = photometric.

^c There are two sources located within the revised XRT error circle. Here we use the redshift of one of them as a proxy for the GRB redshift. The other source, which is a factor of 2 fainter, is likely to reside at an even higher redshift.

^d No emission was detected at wavelengths shorter than 7500Å. This flux “decrement” may be associated with the IGM at $z \approx 5.2$ but could also be associated with a significant reddening of the afterglow.

^e A weak absorption system identified at $z=0.696$ could also be produced by an intervening system and thus the strict redshift range for this GRB would be $0.696 < z < 2.2$.

^f The object is well detected and presents a featureless continuum except for a weak double line

at $z = 1.036$. No other clear features are detected. Therefore, $1.036 < z < 2.7$ is suggested as redshift range for this GRB.

^gGiven the low S/N of the spectrum, this redshift measurement should be considered tentative.

References. — (1) Berger et al. 2005c; (2) Rossi et al. 2014; (3) Berger et al. 2005b; (4) Berger et al. 2005a; (5) Prochaska et al. 2005; (6) Fynbo et al. 2009a; (7) Bloom et al. 2005; (8) Jakobsson et al. 2006; (9) Mirabal et al. 2007; (10) Kawai et al. 2006; (11) Jakobsson et al. 2012; (12) Penprase et al. 2006; (13) Perley et al. 2013a; (14) Grazian et al. 2006; (15) Perley et al. 2013b; (16) Chary et al. 2007; (17) Prochaska et al. 2006; (18) Hjorth et al. 2012; (19) Oates et al. 2009; (20) Berger et al. 2007b; (21) Cucchiara et al. 2007; (22) Krühler et al. 2012; (23) Berger et al. 2007a; (24) Cenko et al. 2007; (25) Thoene et al. 2007; (26) Greiner et al. 2009b; (27) Cucchiara & Fox 2008; (28) Filgas et al. 2008; (29) Krühler et al. 2011a; (30) Fynbo et al. 2008; (31) D’Avanzo et al. 2008; (32) Berger et al. 2008; (33) D’Elia et al. 2008; (34) Krühler et al. 2011b; (35) Chornock et al. 2009a; (36) Levesque et al. 2009; (37) Cucchiara et al. 2011b; (38) de Ugarte Postigo et al. 2009; (39) Levan et al. 2009; (40) Goldoni et al. 2013; (41) Fatkhullin et al. 2009; (42) Jakobsson et al. 2009; (43) Fynbo et al. 2009b; (44) Chen et al. 2009; (45) Chornock et al. 2009b; (46) Rau et al. 2010; (47) Sánchez-Ramírez et al. 2013; (48) Vergani et al. 2010; (49) Kruehler et al. 2013; (50) Flores et al. 2010; (51) Chornock et al. 2010; (52) de Ugarte Postigo et al. 2011; (53) Chornock et al. 2011b; (54) Sparre et al. 2011; (55) Cenko et al. 2011; (56) Cucchiara et al. 2011a; (57) Cabrera Lavers et al. 2011; (58) D’Avanzo et al. 2011; (59) Chornock et al. 2011a; (60) Xu et al. 2013a; (61) Thoene & de Ugarte Postigo 2014; (62) Malesani et al. 2013; (63) Tello et al. 2012; (64) Kruehler et al. 2012a; (65) Cucchiara & Tanvir 2012; (66) Laskar et al. 2014; (67) Xu et al. 2012; (68) D’Elia et al. 2012; (69) Tanvir et al. 2012a; (70) Thoene et al. 2012; (71) Malesani et al. 2012; (72) Sanchez-Ramirez et al. 2012a; (73) Hartoog et al. 2012; (74) Knust et al. 2012; (75) Tanvir et al. 2012b; (76) Kruehler et al. 2012b; (77) Sanchez-Ramirez et al. 2012b; (78) Perley et al. 2012; (79) Fynbo et al. 2013; (80) de Ugarte Postigo et al. 2013; (81) Flores et al. 2013; (82) Cucchiara & Tanvir 2013; (83) Schmidl et al. 2013; (84) Cenko et al. 2013; (85) Castro-Tirado et al. 2013; (86) Smette et al. 2013; (87) Tanvir et al. 2013; (88) Chornock et al. 2013; (89) Xu et al. 2013b; (90) Cucchiara & Cenko 2013; (91) Krühler et al. 2015; (92) Jeong et al. 2014; (93) Chornock et al. 2014b; (94) Tanvir et al. 2014b; (95) Kruehler et al. 2014a; (96) Marshall & Page 2014; (97) Chornock et al. 2014a; (98) Kruehler et al. 2014b; (99) Moskvitin et al. 2014; (100) Castro-Tirado et al. 2014b; (101) Tanvir et al. 2014a; (102) Castro-Tirado et al. 2014a; (103) de Ugarte Postigo et al. 2014; (104) Xu et al. 2014; (105) Gorosabel et al. 2014; (106) de Ugarte Postigo et al. 2015; (107) de Ugarte Postigo & Tomasella 2015; (108) Sanchez-Ramirez et al. 2015; (109) Zheng et al. 2015; (110) Bolmer et al. 2015a; (111) Bolmer et al. 2015b; (112) Xu et al. 2015; (113) Sanchez-Ramirez et al. 2016; (114) Xu et al. 2016; (115) de Ugarte Postigo et al. 2016a; (116) Castro-Tirado et al. 2016; (117) de Ugarte Postigo et al. 2016b; (118) Tanvir et al. 2016; (119) Xu et al. 2017; (120) de Ugarte Postigo et al. 2017b; (121) de Ugarte Postigo et al. 2017c; (122) Izzo et al. 2017a; (123) Malesani et al. 2017; (124) Izzo et al. 2017b; (125) de Ugarte Postigo et al. 2017a; (126) de Ugarte Postigo et al. 2018; (127) Tanvir et al. 2018; (128) Izzo et al. 2018; (129) Selsing et al. 2018; (130) Rossi et al. 2018; (131) Perley et al. 2018;

Table 2. Spectral Parameters

Burst name	Spec. type	t_{start} (s)	ΔT (s)	Model	α	β	E_p (keV)	F (10^{-7} erg cm $^{-2}$ s $^{-1}$)	$\chi^2/\text{d.o.f.}$ (Prob.)
GRB 050126	i	-3.168	38.272	CPL	$-0.90^{+0.28}_{-0.23}$...	158^{+82}_{-41}	$0.63^{+0.19}_{-0.12}$	72.1/59 (0.12)
	p	-0.224	5.888	CPL	$-0.78^{+0.27}_{-0.37}$...	$239^{+2.8}_{-92}$	$1.29^{+0.68}_{-0.61}$	55.5/59 (0.61)
GRB 050219A	i	-5.223	26.496	BAND	$0.02^{+0.19}_{-0.17}$	$-3.35^{+0.55}_{-6.65}$	93^{+6}_{-5}	$2.33^{+0.27}_{-0.25}$	44.5/58 (0.9)
	p	6.553	5.888	CPL	$-0.04^{+0.15}_{-0.14}$...	96^{+4}_{-4}	$2.12^{+0.08}_{-0.07}$	45.0/59 (0.91)
GRB 050315	i	-57.582	85.376	CPL	$0.05^{+0.18}_{-0.18}$...	110^{+7}_{-7}	$4.02^{+0.21}_{-0.19}$	41.6/59 (0.96)
	p	-1.646	8.832	BAND	$-1.41^{+0.19}_{-0.19}$...	47^{+4}_{-4}	$0.59^{+0.04}_{-0.04}$	62.2/59 (0.36)
GRB 050318	i	-0.243	35.328	BAND	$-1.41^{+0.18}_{-0.22}$	$-2.39^{+0.41}_{-7.61}$	113^{+81}_{-32}	$2.33^{+0.53}_{-0.45}$	66.3/58 (0.21)
	p	23.309	8.832	CPL	$-1.54^{+0.18}_{-0.18}$...	132^{+108}_{-37}	$2.12^{+0.52}_{-0.33}$	66.5/59 (0.24)
					$0.11^{+1.47}_{-1.03}$	$-2.24^{+0.10}_{-0.18}$	34^{+8}_{-5}	$0.71^{+0.07}_{-0.07}$	43.1/58 (0.93)
				CPL	$-1.21^{+0.23}_{-0.21}$...	48^{+4}_{-4}	$0.47^{+0.04}_{-0.04}$	45.4/59 (0.9)
				BAND	$-1.17^{+0.24}_{-0.19}$	$-2.60^{+0.29}_{-0.99}$	55^{+5}_{-5}	$1.75^{+0.27}_{-0.28}$	55.1/58 (0.58)
				CPL	$-1.23^{+0.17}_{-0.16}$...	57^{+5}_{-4}	$1.45^{+0.10}_{-0.08}$	56.5/59 (0.57)

Note. — This table is available in its entirety in machine-readable form.

Table 3. Statistics

Parameter	Min ^a	Max ^a	Mean ^a	Median ^a	Min ^b	Max ^b	Mean ^b	Median ^b
Redshift	0.04	9.4	2.4	2.3	0.04	9.4	2.0	1.7
$E_{\text{p},\text{i}}$ (keV)	27	578	144	111	27	3670	238	166
$E_{\text{p},\text{p}}$ (keV)	27	578	171	134	27	3520	282	199
$E_{\text{p},\text{i,z}}$ (keV)	53	2870	509	313	53	6970	650	504
$E_{\text{p},\text{p,z}}$ (keV)	53	2870	596	425	53	6680	768	570
S (10^{-6} erg cm $^{-2}$)	0.1	40.5	6.0	3.9	0.1	3028	62.3	8.0
$F_{\text{peak,64,r}}$ (10^{-6} erg cm $^{-2}$ s $^{-1}$)	0.1	2.9	0.5	0.4	0.1	898	12.9	1.2
E_{iso} (10^{51} erg)	0.03	1477	133	60	0.03	5925	363	86
L_{iso} (10^{51} erg s $^{-1}$)	0	514	41	18	0.002	4632	146	32
θ_{HM} (deg)	1.3	10.2	4.0	3.8	1.3	25.4	5.8	4.5
Coll. factor HM ($\times 10^{-3}$)	0.2	15.8	3.3	2.2	0.2	96.4	7.6	3.0
$E_{\gamma,\text{HM}}$ (10^{50} erg)	0.06	23.2	5.2	1.5	0.06	159.9	15.9	4.7
$L_{\gamma,\text{HM}}$ (10^{50} erg s $^{-1}$)	0.04	2.9	1.0	0.5	0.04	56.0	4.1	1.8

^aFor the sample from this paper.

^bFor the samples from this paper and T17.

Table 4. Burst Energetics

Burst name	z	S^a	$T_{\text{peak},1000}^b$	$F_{\text{peak},1000}^c$	$T_{\text{peak},64}$	$F_{\text{peak},64}$	$T_{\text{peak},64,\text{r}}^b$	$F_{\text{peak},64,\text{r}}$	E_{iso}^d	L_{iso}^e
GRB 050126	1.290	$24.70^{+7.87}_{-5.14}$	4.560	$1.46^{+0.82}_{-0.54}$	3.600	$4.13^{+2.50}_{-1.80}$	4.525	$2.37^{+1.47}_{-1.07}$	$12.15^{+3.87}_{-2.53}$	$2.57^{+1.59}_{-1.16}$
GRB 050219A	0.211	$62.70^{+7.56}_{-7.04}$	9.552	$3.91^{+0.33}_{-0.32}$	9.544	$7.17^{+1.29}_{-1.28}$	9.688	$6.65^{+1.10}_{-1.09}$	$0.76^{+1.09}_{-0.99}$	$0.10^{+0.02}_{-0.02}$
GRB 050315	1.9500	$56.90^{+4.41}_{-4.41}$	4.048	$2.48^{+0.63}_{-0.63}$	4.496	$5.95^{+1.76}_{-1.59}$	4.479	$3.39^{+1.00}_{-1.00}$	$86.89^{+6.73}_{-5.99}$	$13.99^{+4.14}_{-3.75}$
GRB 050318	1.4436	$24.90^{+3.63}_{-3.63}$	28.392	$2.65^{+0.43}_{-0.43}$	28.904	$5.04^{+0.99}_{-0.99}$	28.796	$4.78^{+0.84}_{-0.84}$	$18.39^{+2.68}_{-2.68}$	$8.90^{+1.57}_{-1.57}$
GRB 050505	4.27	$47.40^{+6.73}_{-5.43}$	0.392	$2.97^{+0.84}_{-0.84}$	3.496	$5.39^{+1.93}_{-1.65}$	0.908	$3.39^{+1.03}_{-0.81}$	$192.30^{+2.31}_{-2.31}$	$72.26^{+22.02}_{-17.35}$
GRB 050724	0.258	$9.66^{+2.62}_{-2.62}$	0.000	$6.83^{+1.85}_{-1.92}$	0.008	$31.90^{+8.09}_{-7.77}$	0.025	$28.70^{+7.91}_{-7.91}$	$0.24^{+0.06}_{-0.06}$	$0.88^{+0.24}_{-0.24}$
GRB 050730	3.9693	$187.90^{+88.70}_{-69.40}$	5.152	$3.95^{+1.58}_{-1.58}$	9.592	$11.90^{+6.14}_{-5.03}$	9.553	$6.28^{+3.16}_{-2.56}$	$686.40^{+325.40}_{-254.80}$	$114.70^{+57.65}_{-46.63}$
GRB 050802	1.7102	$70.40^{+12.50}_{-11.50}$	0.080	$9.04^{+1.61}_{-1.61}$	3.568	$14.90^{+4.15}_{-4.08}$	-0.410	$10.30^{+2.71}_{-2.66}$	$62.19^{+11.01}_{-10.19}$	$24.41^{+6.45}_{-6.33}$
GRB 050803	0.422	$86.90^{+21.30}_{-15.90}$	82.000	$1.77^{+0.65}_{-0.46}$	80.456	$3.68^{+1.65}_{-1.36}$	82.688	$3.67^{+1.50}_{-1.17}$	$5.45^{+1.34}_{-1.00}$	$0.29^{+0.12}_{-0.09}$

^aIn units of 10^{-7} erg cm $^{-2}$.

^bThe start time of the time interval, when the peak count rate is reached, s.

^cIn units of 10^{-7} erg cm $^{-2}$ s $^{-1}$

^dIn units of 10^{51} erg.

^eIn units of 10^{51} erg s $^{-1}$.

Note. — This table is available in its entirety in machine-readable form.

Table 5. Collimation-corrected parameters

Burst name	t_{jet} (days)	CBM ^a type	Ref.	θ_{jet} (deg)	Collimation factor ($\times 10^{-3}$)	E_{γ}^{γ} (10^{49} erg)	L_{γ} (10^{49} erg s $^{-1}$)
GRB 050730	0.17 ± 0.02	HM	(1)	1.44 ± 0.07	0.31 ± 0.03	$21.57^{+10.45}_{-8.29}$	$3.60^{+1.85}_{-1.51}$
GRB 050802	0.63	HM	(2)	3.98 ± 0.22	2.41 ± 0.27	$14.98^{+3.15}_{-2.98}$	$5.88^{+1.66}_{-1.66}$
		SWM		3.40 ± 0.16	1.76 ± 0.17	$10.93^{+2.20}_{-2.20}$	$4.29^{+1.20}_{-1.20}$
GRB 050904	2.6 ± 1.0	HM	(3)	3.14 ± 0.32	1.50 ± 0.32	$222.10^{+52.07}_{-55.60}$	$25.70^{+8.18}_{-7.89}$
GRB 051111	0.03 ± 0.01	HM	(1)	1.26 ± 0.11	0.24 ± 0.04	$1.91^{+0.41}_{-0.40}$	$0.43^{+0.10}_{-0.10}$
GRB 060206	1.83 ± 0.09	HM	(1)	4.78 ± 0.07	3.48 ± 0.11	$18.78^{+2.08}_{-2.08}$	$21.73^{+2.83}_{-2.35}$
		SWM		3.93 ± 0.07	2.35 ± 0.09	$12.70^{+1.69}_{-1.43}$	$14.69^{+1.94}_{-1.62}$
GRB 060418	9.49 ± 0.37	HM	(1)	10.20 ± 0.12	15.80 ± 0.37	$232.40^{+15.18}_{-14.51}$	$29.04^{+3.94}_{-3.90}$
		SWM		5.51 ± 0.07	4.62 ± 0.12	$67.99^{+4.59}_{-4.30}$	$8.50^{+1.16}_{-1.14}$
GRB 060526	1.41 ± 0.14	HM	(1)	4.80 ± 0.18	3.51 ± 0.27	$14.35^{+5.12}_{-5.12}$	$24.25^{+8.89}_{-6.46}$
		SWM		4.13 ± 0.23	2.60 ± 0.30	$10.61^{+3.89}_{-3.89}$	$17.93^{+6.75}_{-5.01}$
GRB 060729	0.95 ± 0.14	HM	(1)	7.33 ± 0.33	8.17 ± 0.76	$7.13^{+1.56}_{-1.56}$	$0.79^{+0.27}_{-0.27}$
		SWM		7.08 ± 0.37	7.62 ± 0.83	$6.65^{+2.31}_{-2.31}$	$6.65^{+1.51}_{-1.51}$
GRB 070411	1.76 ± 0.86	HM	(1)	4.53 ± 0.60	3.12 ± 0.87	$48.55^{+22.09}_{-20.98}$	$8.13^{+3.58}_{-3.58}$
		SWM		3.18 ± 0.31	1.54 ± 0.32	$23.92^{+17.18}_{-17.18}$	$4.01^{+1.53}_{-1.53}$
GRB 080310	0.34 ± 0.04	HM	(1)	3.08 ± 0.10	1.45 ± 0.10	$5.36^{+0.90}_{-0.90}$	$1.50^{+0.39}_{-0.39}$
		SWM		3.13 ± 0.10	1.49 ± 0.10	$5.50^{+0.92}_{-0.92}$	$1.54^{+0.32}_{-0.32}$
GRB 081008	0.11 ± 0.01	HM	(1)	1.80 ± 0.05	0.49 ± 0.03	$7.11^{+1.52}_{-1.52}$	$0.76^{+0.19}_{-0.19}$
GRB 090426	0.29 ± 0.07	HM	(1)	4.01 ± 0.27	2.45 ± 0.34	$0.59^{+0.13}_{-0.13}$	$0.86^{+0.04}_{-0.04}$
GRB 091029	0.35 ± 0.08	HM	(1)	2.52 ± 0.16	0.96 ± 0.12	$15.10^{+3.02}_{-3.02}$	$3.30^{+0.75}_{-0.75}$
GRB 110205A	1.19 ± 0.09	HM	(1)	3.54 ± 0.07	1.91 ± 0.08	$120.40^{+10.62}_{-10.00}$	$7.62^{+0.98}_{-0.98}$
		SWM		2.14 ± 0.04	0.70 ± 0.03	$43.83^{+3.77}_{-3.54}$	$2.77^{+0.35}_{-0.33}$

References. — (1) Wang et al. 2018; (2) Kann et al. 2010; (3) Frail et al. 2006;

^aIn cases where the preferred CBM density profile is known, it is taken from the same paper as t_{jet} . Otherwise, calculations for both CBMs are provided and the geometric mean of the HM and WM energetics is used in the calculations.

Table 6. Hardness-intensity correlations

Correlation	N	ρ_S	P_{ρ_S}	a	b	$a_{\sigma_{\text{int}}}$	$b_{\sigma_{\text{int}}}$	σ_{int}
$E_{\text{p,i}}$ versus S	315	0.64	< 0.00001	0.382 ± 0.002	3.89 ± 0.01	0.301 ± 0.017	3.66 ± 0.09	0.217
$E_{\text{p,p}}$ versus F_{peak}	315	0.59	< 0.00001	0.398 ± 0.003	4.41 ± 0.02	0.304 ± 0.019	4.01 ± 0.11	0.234
$E_{\text{p,i,z}}$ versus E_{iso}	315	0.7	< 0.00001	0.429 ± 0.002	-20.18 ± 0.12	0.307 ± 0.016	-13.61 ± 0.87	0.225
$E_{\text{p,p,z}}$ versus L_{iso}	315	0.7	< 0.00001	0.429 ± 0.004	-19.87 ± 0.19	0.310 ± 0.017	-13.59 ± 0.90	0.235
$E_{\text{p,i,z}}$ versus E_{γ}	43	0.57	0.00006	0.566 ± 0.008	-26.01 ± 0.39	0.388 ± 0.066	-16.98 ± 3.36	0.272
$E_{\text{p,p,z}}$ versus L_{γ}	43	0.43	0.004	0.679 ± 0.014	-31.24 ± 0.70	0.269 ± 0.082	-10.71 ± 4.11	0.351

Note. — N is the number of bursts in the fit sample, ρ_S is a Spearman rank-order correlation coefficient, P_{ρ_S} is the corresponding chance probability, a ($a_{\sigma_{\text{int}}}$) and b ($b_{\sigma_{\text{int}}}$) are the slope and the intercept for the fits without (with) intrinsic scatter σ_{int} .

Table 7. LF and EF fits with BPL and Cutoff PL

Data	Evolution (PL index)	Model	α_1	α_2	$\log x_{b,52}$ ($\log x_{\text{cut},52}$)
$\psi(L')$	$\delta_L=1.2$	BPL	$-0.28^{+0.04}_{-0.07}$	$-1.01^{+0.10}_{-0.28}$	$0.21^{+0.28}_{-0.18}$
$\psi(L')$	$\delta_L=1.2$	CPL	$-0.45^{+0.08}_{-0.01}$...	$1.67^{+0.49}_{-0.44}$
$\psi(E')$	$\delta_E=1.1$	BPL	$-0.29^{+0.01}_{-0.09}$	$-1.01^{+0.02}_{-0.44}$	$0.80^{+0.44}_{-0.06}$
$\psi(E')$	$\delta_E=1.1$	CPL	$-0.35^{+0.03}_{-0.04}$...	$1.74^{+0.07}_{-0.11}$
$\psi(L_{\text{iso}})$	no evolution	BPL	$-0.26^{+0.02}_{-0.05}$	$-0.99^{+0.05}_{-0.17}$	$0.78^{+0.17}_{-0.08}$
$\psi(L_{\text{iso}})$	no evolution	CPL	$-0.38^{+0.04}_{-0.03}$...	$2.02^{+0.11}_{-0.19}$
$\psi(E_{\text{iso}})$	no evolution	BPL	$-0.26^{+0.01}_{-0.08}$	$-0.97^{+0.03}_{-0.44}$	$1.24^{+0.46}_{-0.08}$
$\psi(E_{\text{iso}})$	no evolution	CPL	$-0.32^{+0.02}_{-0.04}$...	$2.21^{+0.06}_{-0.09}$